

Article

Exploring the Performance Boundaries of a Small Reconfigurable Multi-Mission UAV through Multidisciplinary Analysis

Dioser Santos ^{1,†} , Jeremy Rogers ^{1,2,†} , Armando De Rezende ^{1,3,†}  and Victor Maldonado ^{1,*,†}

¹ Flow Control and Aerodynamics Lab, Department of Mechanical Engineering, Texas Tech University, Lubbock, TX 79409, USA; dioser.santos@ttu.edu (D.S.); jeremy.rogers@SRNL.doe.gov (J.R.); armando.rezende@ttu.edu (A.D.R.)

² Savannah River National Laboratory, Aiken, SC 29808, USA

³ Combustion Lab, Department of Mechanical Engineering, Texas Tech University, Lubbock, TX 79409, USA

* Correspondence: victor.maldonado@ttu.edu

† These authors contributed equally to this work.

Abstract: The performance of a small reconfigurable unmanned aerial vehicle (UAV) is evaluated, combining a multidisciplinary approach in the computational analysis of additive manufactured structures, fluid dynamics, and experiments. Reconfigurable UAVs promise cost savings and efficiency, without sacrificing performance, while demonstrating versatility to fulfill different mission profiles. The use of computational fluid dynamics (CFD) in UAV design produces higher accuracy aerodynamic data, which is particularly important for complex aircraft concepts such as blended wing bodies. To address challenges relating to anisotropic materials, the Tsai–Wu failure criterion is applied to the structural analysis, using CFD solutions as load inputs. Aerodynamic performance results show the low-speed variant attains an endurance of 1 h, 48 min, whereas its high-speed counterpart is 29 min at a 66.7% higher cruise speed. Each variant serves different aspects of small UAS deployment, with low speed envisioned for high-endurance surveying, and high speed for long-range or time-critical missions such as delivery. The experimental and simulation results suggest room for design iteration, in wing area and geometry adjustments. Structural simulations demonstrated the need for airframe improvements to the low-speed configuration. This paper highlights the potential of reconfigurable UAVs to be useful across multiple industries, advocating for further research and design improvements.

Keywords: unmanned aerial vehicle; reconfigurable; multi-mission; computational fluid dynamics; additive manufacturing; finite element analysis



Citation: Santos, D.; Rogers, J.; De Rezende, A.; Maldonado, V. Exploring the Performance Boundaries of a Small Reconfigurable Multi-Mission UAV through Multidisciplinary Analysis. *Aerospace* **2023**, *10*, 684. <https://doi.org/10.3390/aerospace10080684>

Academic Editor: Gokhan Inalhan

Received: 18 May 2023

Revised: 23 July 2023

Accepted: 26 July 2023

Published: 31 July 2023



Copyright: © 2023 by the authors. Licensee MDPI, Basel, Switzerland. This article is an open access article distributed under the terms and conditions of the Creative Commons Attribution (CC BY) license (<https://creativecommons.org/licenses/by/4.0/>).

1. Introduction

At present, unmanned aerial vehicles (UAVs) are primarily used for data gathering, remote sensing, and observation tasks in a variety of sectors, such as photography, logistics, telecommunications, agriculture, search and rescue, disaster management, infrastructure inspection, and entertainment [1–6]. They can provide safe operation in dangerous environments and enable access to remote locations, normally at low cost. Recent advances in wireless networks [7] and artificial intelligence [8] allow intense progress in sensing and communication, and equivalent progress in the UAV mission capabilities is required. Although the available software is capable of performing all types of tasks, normally a different aircraft is required for each mission [9]. Therefore, a reconfigurable UAV can be devised for different tasks, capable of performing them at high performance. This offers a great advantage over systems designed for a single specific mission because different setups can provide enhanced performance at different mission profiles. Moreover, the use of a reconfigurable UAV has been seen to provide a 26% cost reduction with respect to off-the-shelf products [10].

The development of a family of reconfigurable UAVs includes the enhancement of interchangeable components, such as wings, tails, engines, and payloads, improving the performance of each type of mission and the overall flexibility of the family [11]. The goal of the Switchblade UAV design is to combine the flexibility of reconfigurable vehicles with the performance of optimized components, as envisioned in previous works [12,13]. The Switchblade is a small unmanned aerial system (UAS) concept that adopts a hybrid role in the form of two main aircraft variants for long-endurance, slow-flight, or long-range fast operation. This is intended to provide a variety of mission profiles at a reduced cost.

Recent literature on UAV design revealed that when it comes to reconfigurability, most cases refer to morphing wings, fixed-wing aircraft with VTOL capabilities, hybrid multi-domain vehicles, or arrays of multiple UAVs connected to each other. A gap exists in the design of modular reconfigurable UAVs envisioned for drastically different mission requirements, and this work aims to fill it. Table 1 shows recent designs in the field and how they compare to Switchblade with their key parameters.

Table 1. Comparison of recent (2020–2023) literature to the current project.

Paper	Variant or Type	Manufacture	Wing Airfoil	Materials	Endurance	Cruise Speed	Range	L/D
Adawy [14]	Fixed wing	Laser cut, foam cutting	E423	Balsawood Plywood Aluminum		14.5 m/s		
Ayele [15]	Inflatable wing		E180	Polyurethane blade UV-sensitive woven material	0.34 h	158.21 m/s		13.8
Chu [16]	Max. Extension			N/A		16 m/s		21.5
	Transition					17 m/s		19.9
	Min. Extension					18 m/s		19
Elelwi [17]	100% span length		NACA 4412			51 m/s	102 km	23.76
	125% span length		NACA 4412			51 m/s	120 km	26.5
	150% span length		NACA 4412			51 m/s	130 km	29
	175% span length		NACA 4412			51 m/s	150 km	32.35
Gatto [18]	Active twist control	Laser Cut	Variable	Balsawood Plywood Fiberglass		18–25 m/s		9.8–10.66
Goetzendorf-Gabowski [19]	Fixed wing VTOL		S4062-095-87		1.5 h	22 m/s		14.3
Kim [20]	Multi-UAV Array	Assembled Components	N/A	Various	0.17 h			
	Individual UAV	Assembled Components	N/A	Various	0.17 h			
Lu [21]	Air	Off-the-shelf Components		Carbon fiber		31.5 m/s		3.92
	Water	Off-the-shelf Components		Carbon fiber			Depth 50 m	
Lyu [22]	Air	Off-the-shelf Components		Composite	0.17 h			
	Water	Off-the-shelf Components		Composite	0.37 h	0.5 m/s	Depth 25 m	

Table 1. Cont.

Paper	Variant or Type	Manufacture	Wing Airfoil	Materials	Endurance	Cruise Speed	Range	L/D
Santos	LSHE	3D printed	E171/E330	Nylon 12 CF	1.8 h	20.16 m/s	131 km	18.2
	HSLR	3D printed	E171//E182	Nylon 12 CF	0.49 h	33.62 m/s	59 km	16.2
Savastano [23]	Flapping wing		AS-6091	Ultralight fabric		11 m/s		76
Wong [24]	Fixed wing VTOL	Foam cutting	MH 78	polystyrene woven glass fiber				4

The application of additive manufacturing methods in the aircraft industry is widespread and offers many advantages in the production of parts, such as shortened production cycle times, reduction in costs, lighter component weights, and even the globalization of the aircraft industry [25–27]. Additionally, 3-D printing can be used for efficient production of wind tunnel models, a task that is usually time-consuming and costly [28–30]. Additive manufacturing has been used in the production and experimental evaluation of wings in the transonic regime by [31]. Similarly, the concept of a bio-inspired morphing UAV model has been manufactured and tested in [30]. In this work, one of the goals is to take full advantage of additive manufacturing for prototyping and testing purposes; however, there are still challenges related to the use of this technology for aircraft structures, such as the low strength of fused deposition modeling (FDM) materials, anisotropy, porosities, manufacturing process variability, and imperfections that can be critical to thin-walled features [32,33]. It is necessary to address these issues when designing aircraft structures for safe operation and full life cycles.

The outstanding development of computational fluid dynamics (CFD) software and computational resources in the last couple of decades has benefited the aircraft industry [34–36], and by association, UAV designers [37]. CFD methods are increasingly used in the early stages of UAV design, with varying fidelity depending on the level of development [15,38]. Extensive analyses with RANS, URANS, and DES simulations have been performed on an unmanned combat aerial vehicle (UCAV), resulting in accurate prediction of vortical flow over a delta wing configuration [39]. Determination of the dynamic stability characteristics of an aircraft—a task that is normally difficult to predict with numerical simulations and usually accomplished empirically or experimentally—was successfully executed in [40], where CFD results had great correlation with flight test data. Dynamic stability derivatives for an airfoil were obtained in [41], also with a good correlation of experimental data. Even the use of active and passive flow control methods applied to UAV performance enhancement has been studied in computational frameworks [42–44]. The use of higher fidelity CFD models and simulations for the Switchblade UAV is critical to obtain higher accuracy aerodynamic data and to evaluate the performance of both variants: low-speed high-endurance (LSHE) and high-speed long-range (HSLR). Moreover, in this study, CFD work serves to inform the structural analysis and wind tunnel experiments by giving essential input to FEA studies and is a basis for comparison to experimental results.

The design of a UAV is a complex process, involving different disciplines such as aerodynamics, propulsion, structural integrity, stability and control, electronics, communication, and manufacturing techniques. Moreover, the reconfigurable nature of Switchblade promotes the integration of conflicting features in the same system, i.e., high-speed long range and low-speed high endurance. Therefore, a multidisciplinary collaboration is applied to the project, combining design and numerical analysis to enhance the performance and safety of the different modules in both aerodynamic (CFD) and structural (FEA) criteria. Finally, wind tunnel testing of the different configurations provides experimental validation and the comparison with computational models to provide a more complete understanding of the system. The methodology used here is an extension of a previous work [12] and is explained in Section 2.1.

1.1. Background

Previous design efforts have been made to develop a family of unmanned aerial vehicles that inherit a unique reconfigurability feature to allow multiple missions of different regimes using the same unmanned aerial system (UAS). This UAS is to be referred to as ‘Switchblade’ and offers a vehicle with a modular framework assuming one of four variants based on the mission requirements. The scope of the Switchblade project is to obtain a balance between flight performance and wide-mission adaptability, providing an economic advantage in that only a single UAS is needed by an operator.

The conceptual design framework for Switchblade was previously conducted in [12]. Considering a variety of missions in commercial sectors in which UAVs are utilized, as shown in Table 2, three different mission profiles were studied to examine the required flight performance, resulting in four distinguishable UAV variants (Figure 1). In surveillance and inspection-type missions, Switchblade is loaded with a high-resolution camera payload, contained in its transparent nose and weighing up to 0.3 kg. For inspections, the UAV is required to accumulate up to 30 min in hover, which was considered in the conceptual design phase for battery sizing. In delivery missions, the fastest variant (HSLR) is deployed, carrying a payload of up to 0.5 kg. The VTOL capability is crucial in this application to reduce the space needed for take-off and landing. The HSLR variant without VTOL is also able to perform surveillance in time-critical situations, reaching points of interest in a shorter time due to its 66% higher cruise speed.

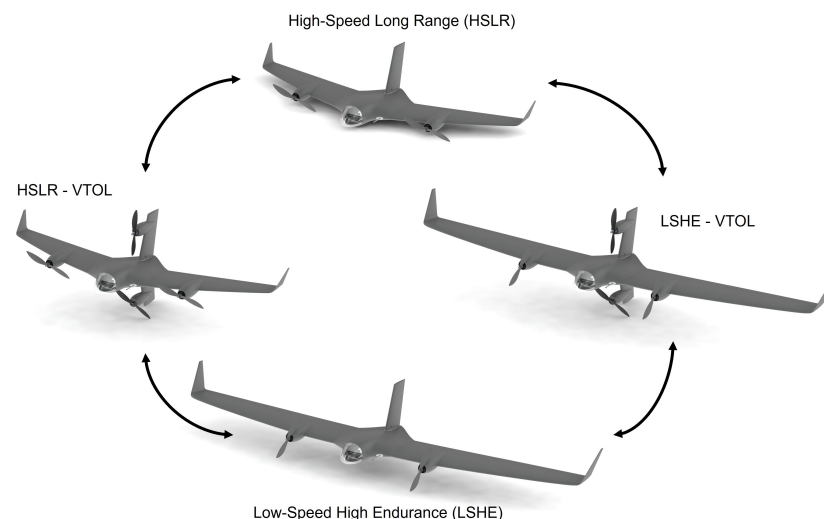


Figure 1. Switchblade multi-mission variants.

Table 2. Initial mission performance requirements, adapted from [12].

Mission	Performance	Range	Cruise Mach	VTOL	Payload	Weight
Surveillance	LSHE	200 km	0.06	No	Camera	3.93
Delivery	HSLR-VTOL	100 km	0.1	Yes	Package	4.66
Inspection	LSHE-VTOL	37 km	0.06	Yes, 30 min	Camera	4.50

The Switchblade UAS consists of a blended wing body (BWB) acting as the common module among all UAV variants, connecting to wing modules. Tailless aircraft have many advantages over traditional aircraft, such as lower weight and drag, smaller cross sections, and higher aerodynamic efficiency [45]. Figure 1 shows the Switchblade family concept. The ‘parent’ UAV variant is the high-speed long-range (HSLR) variant which is prioritized in the design process due to its higher cruise speed and, thus, higher propulsion demand. The low-speed high-endurance (LSHE) variant is the ‘child’ variant, where its propulsion demand is automatically satisfied. Both variants can be enabled for vertical take-off and landing (VTOL) by exchanging their vertical stabilizer with two removable fins that

contain electric motor propulsion units. All of the modules are integrated into a Pixhawk flight controller system, chosen for its vast open-source documentation and configuration flexibility. It recognizes the given module combination to adjust flight control parameters accordingly, i.e., in the case that HSLR-VTOL is the current setup, the flight controller loads the appropriate settings for a vertical take-off and landing high-speed flight.

1.2. Research Objectives

The overarching goal of this work is to push the boundaries of reconfigurable design with consideration to the aerodynamics and structural integrity of two UAV variants designed with functional 3-D printed materials and with significantly different cruise speeds. Both the HSLR and LSHE variants utilize the same BWB, and the notion of reaching a reconfigurable design 'boundary' is defined in this study as when one of the two variants begins to perform considerably sub-optimally during simulated flight. This notion is discussed throughout the computational and experimental results. The performance criteria considered are: (i) the aerodynamic efficiency and (ii) the structural minimum factor of safety (FoS) and deformation.

The first objective is to carry out a refined CFD analysis of the UAV variants, giving continuity to the work performed during the conceptual design phase in [12]. This is accomplished by more detailed geometries, larger fluid domains, and finer meshes. The second objective is to identify maximum stress locations and magnitudes through FEA. Considering that the Switchblade prototypes are manufactured by advanced 3-D printing processes almost in their entirety, it is crucial to acknowledge that manufacturing imperfections or defects may occur and that high stresses are identified and mitigated. However, the use of newly introduced commercial materials, such as carbon fiber-reinforced nylon, may present a challenge to aircraft prototyping because UAV structures can be very thin at certain locations, and, therefore, particularly susceptible to manufacturing imperfections that reduce the strength and/or stiffness [33].

Finally, the third objective is to test the Switchblade prototypes in a wind tunnel. In this investigation, the main experimental results sought are aerodynamic coefficients at static angles of attack. The secondary aims are to assess the control surface and propulsion performance. A modular half-body model is used to test the LSHE and HSLR wing designs. One particular challenge is the complex geometry of the wings, in which each configuration contains three different airfoils throughout the wing. Additionally, most of the empirical formulations for aerodynamic parameters are developed for large-scale aircraft, and the lower Reynolds number of UAVs in the laminar and transitional flow regime may cause the empirical and computational results to be less accurate than expected, making wind tunnel testing even more important.

2. Materials and Methods

2.1. Multidisciplinary Approach

The development of the UAV family began in the conceptual design framework shown in a previous work [12]. Part of that framework is contained in the flowchart of Figure 2. The initial inputs are parameters related to the different missions to be accomplished, such as range, cruise speed, payload, and the use of vertical take-off and landing (VTOL), as discussed in Section 1.1. They are used to generate different aircraft configurations capable of achieving the missions. A minimum number of modules is extracted from the configurations, such as wings and stabilizers, and, in the product platform planning phase, are modeled and analyzed with low-order methods, considering performance and failure criteria. An in-depth explanation of the modular product platform planning method is presented in [10]. The result is the initial aerodynamic sizing of a minimum number of feasible variants and the starting point for high-order analysis. The aircraft geometries are modeled with CFD (Section 2.2) and improved iteratively until the desired performance is achieved. The structural design follows the establishment of an external geometry, and the airframe is analyzed with FEA (Section 2.3) taking inputs from CFD simulations.

The structure is improved iteratively until factors of safety are acceptable. The feedback loops in the disciplines of aerodynamics and structures ensure that high-order methods correct decisions taken from low-order solutions. After that, models are manufactured and prepared for wind tunnel experimentation, as in Section 2.4. The experimental results are then compared to CFD to validate the model. Ultimately, a prototype is manufactured for flight testing.

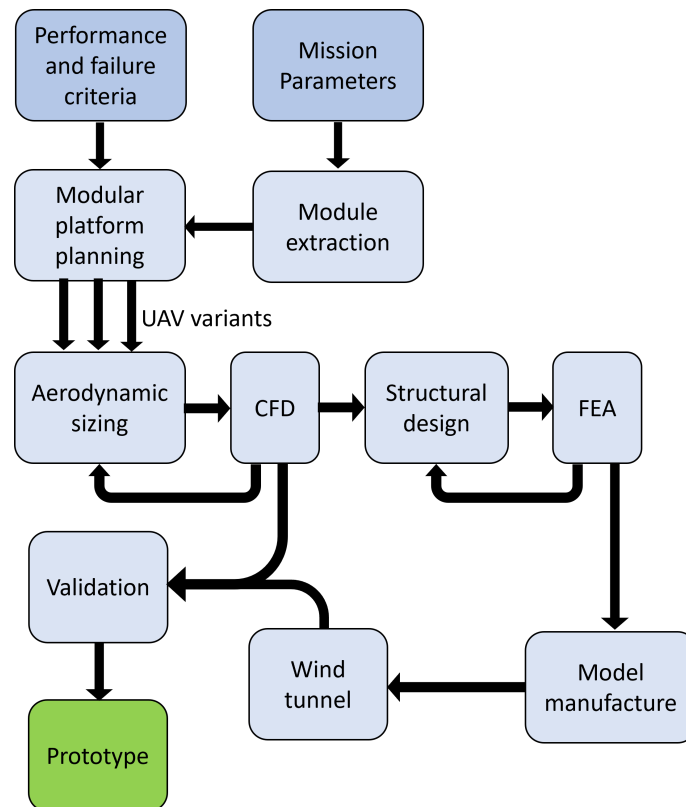


Figure 2. Multidisciplinary approach.

2.2. Computational Fluid Dynamics Studies

2.2.1. CFD Geometries

The wing geometries used for the CFD studies were based on two main variants—low-speed high-endurance (LSHE) and high-speed long-range (HSLR)—according to the multi-mission ideas explored in the conceptual design phase (Figure 1). Although Switchblade can be enabled for vertical take-off and landing (VTOL), this analysis focuses on the standard forward flight configurations. Within these two variants, different CAD versions were created to analyze the effect of geometry complexity on aerodynamic results. The “clean wing” versions consist of the center blended wing body (BWB) geometry connected to its respective wing panels depending on mission type—LSHE or HSLR. The “actual wing” versions consist of the same center body geometry but are connected to wing panels that contain motor nacelles and winglets, and, therefore, more closely resemble the aircraft in its final configuration. For nomenclature reasons, the “clean wing” models and their associated geometries are named LSHE and HSLR, while the “actual wing” versions are named LSHEWN and HSLRWN. The “W” and “N” refer to “winglet” and “nacelle”, respectively. Figure 3 shows the geometries used for the CFD simulations.

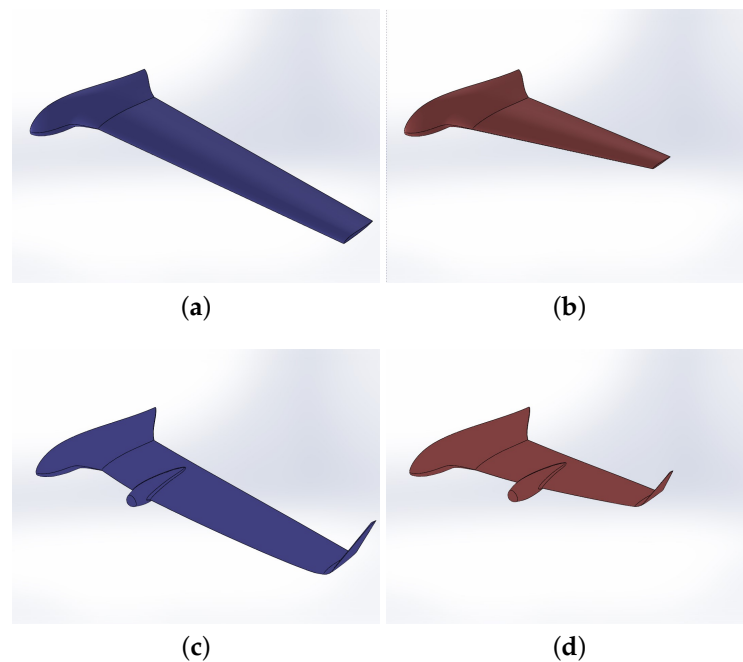


Figure 3. (a) LSHE; (b) HSLR; (c) LSHEWN; (d) HSLRWN.

The reconfigurability of Switchblade signifies that some airfoils are shared between different variants. The center body is designed from an MH 81 reflex airfoil, modified to attain a maximum thickness ratio of 20% for increased internal volume required for electronics. The interface between the center body and the wing panel—the wing root—was designed with a symmetric airfoil, and each wing panel has a different wing tip airfoil. Both variants have reflex airfoils at the wing tip, with LSHE having a more significant reflex to compensate for its lower wing sweep. The airfoils used in each variant and wing characteristics are shown in Tables 3 and 4, respectively.

Table 3. Wing airfoil characteristics.

UAV Variant	Location	Airfoil	Thickness, % <i>c</i>	Camber, % <i>c</i>	C_{D_o}
LSHE	Root	Eppler 171	12.28	0	0.008
LSHE	Tip	Eppler 330	11	2.1	0.01
HSLR	Root	Eppler 171	12.28	0	0.008
HSLR	Tip	Eppler 182	8.5	1.2	0.007

Table 4. Wing characteristics.

UAV Geometry	S [m ²]	A	Span, b [m]	Sweep, Λ	Taper Ratio, λ
LSHE	0.476	9.7	2.15	7.8°	0.53
HSLR	0.309	6.6	1.43	24°	0.35
LSHEWN	0.488	9.5	2.15	7.8°	0.53
HSLRWN	0.324	6.3	1.43	24°	0.35

In preparing the wing geometries for meshing, some practices were followed to ensure that mesh generation would run smoothly, therefore facilitating convergence and good results. Rounding the wing trailing edges into fillets was revealed to be critical in improving mesh quality, and a radius value between 0.2% and 0.4% of the local wing chord was used, depending on the geometry. Sectioning surfaces into areas separated by leading and trailing

edges and chord regions improved meshing by providing the software with edges to seed element nodes.

In each case, half of the aircraft wing body was analyzed, taking advantage of the symmetric flow field to reduce the time to achieve a converged solution. The size of the fluid domain needs to be sufficiently large so that the far field of the fluid surrounding the wing does not interfere with the physical flow phenomena close to the wing. To achieve this, the fluid domain dimensions were defined using the recommendations from [46] to have at least 25 body lengths around a three-dimensional aircraft. The fluid domain consisted of a half-elliptical volume with a semi-major axis of 26 m and a minor axis of 26 m, illustrated in Figure 4. These dimensions have increased dramatically since early CFD simulations were conducted. The nose of the airplane is located at the center of the semi-major axis and faces the upstream direction, towards the elliptical surface.

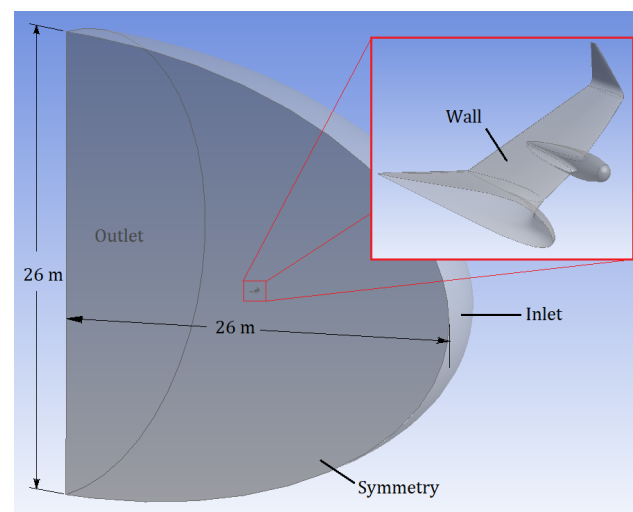


Figure 4. Fluid domain in CFD simulations.

2.2.2. CFD Meshes

The CFD studies performed after the conceptual and preliminary analyses in [12] were characterized by finer meshes with a drastic increase in the number of cells in the fluid domain. This was completed primarily to generate a better discretization of the regions close to the wall boundaries. Whereas in the conceptual study, the mesh size was below 3.4 million cells, in this study, some meshes surpassed the 15 million cell mark. This was accomplished, in part, by utilizing mosaic-meshing in ANSYS fluent meshing. This meshing method incorporates poly-hexcore cells and is characterized by filling the bulk volume geometry with hexahedral elements while filling areas with more complex geometries, especially near the wing surface, with polyhedral elements. Mosaic mesh is able to connect the hexahedral and polyhedral elements to one another, thereby incorporating the best parts of each element into every section of the geometry [47]. The result is a more efficient mesh that carefully resolves the boundary layers, capturing flow variables more accurately. Emphasis was given to first-cell height at the wall boundaries, with the goal of obtaining y^+ values in the order of one to accurately resolve the viscous sub-layer, a practice well discussed by [46,48]. To estimate the first cell height, Equations (1a) to (1d) were used

$$Re_x = \frac{\rho V_\infty L}{\mu} \quad (1a)$$

$$C_f = \frac{0.026}{Re_x^{\frac{1}{2}}} \quad (1b)$$

$$\tau_w = \frac{C_f \rho V_\infty^2}{2} \quad (1c)$$

$$\Delta S = \frac{y^+ \mu}{\sqrt{\frac{\tau_w}{\rho}} \rho} \quad (1d)$$

where Re_x is the Reynolds number, ρ is the air density, V_∞ is the free-stream velocity, L is the reference length (the mean aerodynamic chord), μ is the air dynamic viscosity, C_f is the skin friction coefficient, τ_w is the wall shear stress, and ΔS is the first cell height to be determined. From these calculations, the estimate of the first cell height was approximately 0.01 mm. To reduce the mesh cell count, a value of 0.05 mm was implemented. From the first cell at the wall, 25 to 30 inflation layers were created, depending on the final number of cells in the model.

To the extent possible, meshes were generated with at least a hundred cells across the minimum chord length (excluding the winglet), a guideline based on common CFD practices. This meant computing the average face size for the wall boundaries from the mean aerodynamic chord of both variants and making adaptations to reduce the computational cost of calculations. Details about the meshes used in the CFD work are presented in Table 5. Wall faces refer to the number of polygonal faces generated on the aircraft surface. The mesh quality measure used was orthogonal quality. Figure 5 shows a mesh example for the HSLRWN geometry.

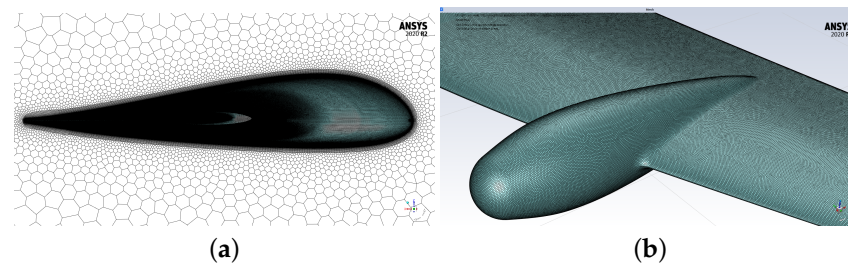


Figure 5. (a) Mesh at symmetry boundary; (b) mesh at wall boundary close to the nacelle.

Table 5. Mesh summary.

Model	Cells	Nodes	Wall Faces	Quality	Face Size	Inflation
LSHE	9.9×10^6	22.1×10^6	2.6×10^5	0.20	2 mm	30
HSLR	15.5×10^6	34.9×10^6	4.1×10^5	0.11	1 mm	30
LSHEWN	6.1×10^6	14.1×10^6	1.8×10^5	0.11	3 mm	25
HSLRWN	15.0×10^6	34.0×10^6	4.6×10^5	0.19	1 mm	25

2.2.3. CFD Turbulence Method and Flow Conditions

The turbulence model used for the simulations was the $k-\omega$ shear stress transport (SST) model. It was chosen for its capability to accurately model boundary layer flow and non-sensitivity to free-stream conditions [49]. The $k-\omega$ SST model provides a hybrid, robust approach to turbulence formulation as it uses the $k-\omega$ model in the near-wall region and incorporates the $k-\epsilon$ model in the free-stream far field. However, the $k-\omega$ model can be sensitive to inlet velocity boundary conditions leading to inaccurate turbulence formulation [50]. To avoid this issue, the $k-\omega$ SST model switches to the $k-\epsilon$ model in the far-field regions of the fluid domain. This model solves two transport equations that are

dependent on the turbulent kinetic energy, k , and the specific turbulence dissipation rate, ω , shown in Equations (2) and (3), respectively [51].

$$\frac{\partial}{\partial t}(\rho k) + \frac{\partial}{\partial x_i}(\rho k u_i) = \frac{\partial}{\partial x_j} \left(\Gamma_k \frac{\partial k}{\partial x_j} \right) + \tilde{G}_k - Y_k + S_k \quad (2)$$

$$\frac{\partial}{\partial t}(\rho \omega) + \frac{\partial}{\partial x_i}(\rho \omega u_i) = \frac{\partial}{\partial x_j} \left(\Gamma_\omega \frac{\partial \omega}{\partial x_j} \right) + G_\omega - Y_\omega + D_\omega + S_\omega \quad (3)$$

Here, Γ_k is the effective diffusivity of k , \tilde{G}_k is a generation term for turbulence kinetic energy due to mean velocity gradients, Y_k is the dissipation of k , and S_k is a source term. Γ_ω is the effective diffusivity of ω , Y_ω is the dissipation of ω , and D_ω is a cross-diffusion term.

For the steady state, the inlet conditions were adjusted with flow velocity set at 33.62 m/s for the high-speed design cruise speed and 20.16 m/s for the low-speed model. The inlet turbulence intensity was set at 1%, a reasonable amount for undisturbed atmospheric conditions. The outlet condition is set at a gauge pressure of zero. Convergence criteria were applied to the residuals to improve the simulation time and results. The convergence requirement for the velocity components, k , and omega residuals was set to 10^{-5} , and the continuity residual was set to 10^{-3} . For the monitored quantities—lift, drag, and pitching moment—the convergence criterion was set to 10^{-3} .

2.3. Finite Element Analysis Studies

The challenges with 3-D printed materials arise from the lack of consistency, and 3-D printed materials can differ from model to model due to variables such as printing direction and fill density. For instance, in Gu et al's publication on composite structures, there is an increased risk due to the complexity from high anisotropy and a variety of failure modes [52]. For simplicity, the Von Mises failure criterion is commonly used on 3-D printed materials, however, it assumes the material to be isotropic [52]. In this study, the Tsai–Wu failure criterion was more suitable since 3-D printed and composite materials are inherently anisotropic, and Tsai–Wu is a generally acceptable failure criterion for anisotropic materials. The FEA analysis was performed using ANSYS to identify stresses and locations where the wing is more likely to fail.

2.3.1. FEA Geometry

In the FEA investigation on the reconfigurable UAV design, it is important to highlight the key techniques used in modeling the geometry for the static structural analysis in the ANSYS workbench. The solid model of each variant (LSHE and HSLR) was provided by *Stratasys*, and, from these models, the internal structure, wing skin, and winglets could be modeled for the static structural simulation. The models were shelled out, and an internal structure was designed with ribs and shear webs. The CAD drawing of the prototype manufactured is shown in Figure 6a. The wing module connects to the center body via two tubular carbon fiber spars and is locked in place with a spring mechanism. The wing structure analyzed is shown in Figure 6b.

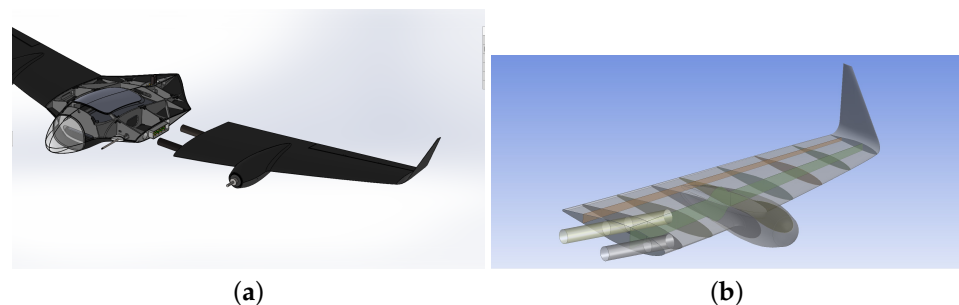


Figure 6. (a) HSLR assembly detail; (b) HSLR wing structure.

2.3.2. Material Properties

Nylon 12 CF was used for 3-D printing and testing of the Switchblade aircraft. This material consists of a polymer matrix (nylon) containing short carbon fibers predominantly oriented in the print bead direction. For the finite element analysis of the aircraft, the material was modeled as a representative volume element (RVE) in ANSYS with Material Designer, which calculated the elastic constants necessary for the orthotropic material. Figure 7a shows the macrostructure of the printed material surface, which was used as a basis for modeling the RVE shown in Figure 7b.

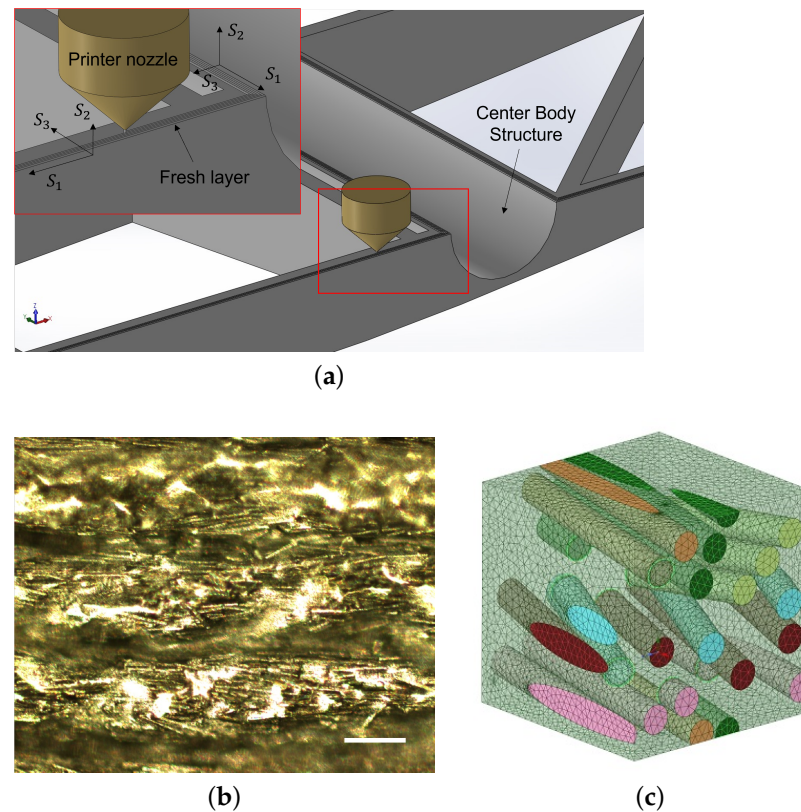


Figure 7. (a) Printing direction relationship with stress components; (b) surface profile taken at 10× magnification, scale bar is 140 μm; (c) representative volume element.

The material strength limits were obtained from *Stratasys* [53]. Nylon 12 CF properties differ depending on its printing direction, therefore when modeling the material in ANSYS, its property directions were defined similarly to composite laminates, where 1 is the fiber direction (or the print bead direction), 2 is across fibers (same as the print layering direction), and 3 is the out-of-plane direction (or across the beads). This was performed to allow for orientation of the material according to the way it is printed throughout the structure components.

Considering the orthotropic properties of the nylon 12 CF material, it was critical that a failure criterion better suited to this material was used in the setup model in ANSYS. The chosen failure criterion was the Tsai–Wu criterion of composite materials. Chen et al. [54] have used the Tsai–Wu failure criterion in their analysis of a 3-D printed bracket made of polylactic acid. The Tsai–Wu failure criterion is introduced in Equation (4)

$$H_1\sigma_1 + H_2\sigma_2 + H_{11}\sigma_1^2 + H_{22}\sigma_2^2 + H_{66}\tau_{12}^2 + 2H_{12}\sigma_1\sigma_2 < 1 \quad (4)$$

where the constants H_1 , H_{11} , H_2 , H_{22} , H_{66} , and H_{12} are dependent on the strength terms of the material in many directions, as seen in Equations (5a) to (5f). σ_1 is the normal stress in

the printing bead direction, σ_2 the normal stress across the beads and in-plane, and τ_{12} the plane shear stress.

$$H_1 = \frac{1}{(\sigma_1^T)_{ult}} - \frac{1}{(\sigma_1^C)_{ult}} \quad (5a)$$

$$H_{11} = \frac{1}{(\sigma_1^T)_{ult}(\sigma_1^C)_{ult}} \quad (5b)$$

$$H_2 = \frac{1}{(\sigma_2^T)_{ult}} - \frac{1}{(\sigma_2^C)_{ult}} \quad (5c)$$

$$H_{22} = \frac{1}{(\sigma_2^T)_{ult}(\sigma_2^C)_{ult}} \quad (5d)$$

$$H_{66} = \frac{1}{(\tau_{12})_{ult}^2} \quad (5e)$$

$$H_{12} = -\frac{1}{(\sigma_1^T)_{ult}^2} \quad (5f)$$

In the Tsai–Wu H -constants, $(\sigma_1^T)_{ult}$ and $(\sigma_1^C)_{ult}$ are the ultimate tensile and compressive strengths of a composite lamina in the fiber direction “1”, respectively. $(\sigma_2^T)_{ult}$ and $(\sigma_2^C)_{ult}$ are the ultimate tensile and compressive strengths in the direction across the fibers “2”, and $(\tau_{12})_{ult}$ is the ultimate shear stress of the lamina.

2.3.3. FEA Meshes

A quadrilateral-dominant mesh was used to discretize the wing geometry, with a target mesh size of 3 mm in the wing surface. This size was chosen specifically to bring the FEA mesh close to the CFD surface grid on the wing, facilitating the interpolation of the pressure data into the FEA model. The mesh for the high-speed long-range aircraft is shown in Figure 8. Mesh information for both variants is summarized in Table 6.

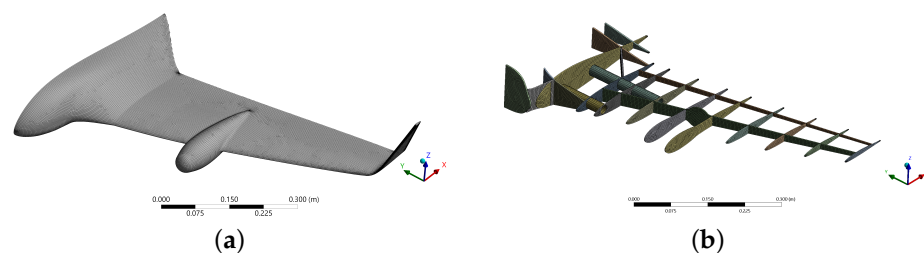


Figure 8. (a) HSLR Surface FEA Mesh; (b) HSLR internal structure.

Table 6. FEA Mesh Summary.

Aircraft Model	Target Size	Elements	Nodes	Min. Quality	Average Quality
LSHE	3 mm	180,647	157,269	0.041	0.893
HSLR	3 mm	157,401	132,626	0.044	0.887

2.3.4. Load and Boundary Conditions

To determine loading in the FEA simulation, V-n diagrams of the HSLR and LSHE models were constructed, considering a positive limit load factor of 3, within the acceptable range described in FAR Part 23 [55]. Loading cases in this work were limited to positive G,

symmetrical maneuvers. The geometry of the aircraft and design performance parameters were used to calculate points of interest for the analysis using Equation (6)

$$V_A = \sqrt{\frac{2n_{max}(\frac{W}{S})}{\rho C_{L,max}}} \tag{6}$$

where V_A is the corner speed for each variant, and n_{max} is the limit load factor considered. W is the aircraft weight, S is the wing reference area, and $C_{L,max}$ is the maximum lift coefficient. The maximum speed V_D was considered as $1.5 \times$ cruise speed, also following FAR Part 23 guidance [55]. The V-n diagrams for each variant are shown in Figure 9. From the V-n diagram data, the speed and angle of attack at each flight condition were calculated. The results are elaborated on in Table 7.

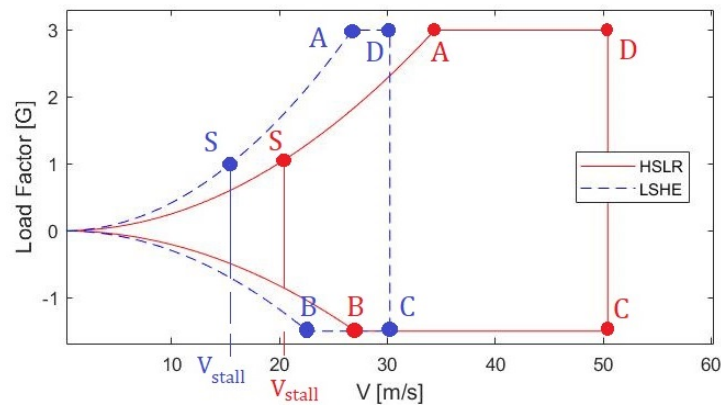


Figure 9. Maneuver diagram for Switchblade variants.

Table 7. V-n diagram results for HSLR and LSHE variant.

Variant	Analysis Point	Airspeed [m/s]	Angle of Attack [°]	C_L
HSLR	A	$V_A = 34.42$	12.0	0.584
HSLR	D	$V_D = 50.43$	3.2	0.272
LSHE	A	$V_A = 26.75$	11.0	0.619
LSHE	D	$V_D = 30.24$	6.4	0.549

These parameters are then used as inputs in a dedicated CFD simulation to generate the pressure field over the wing surface. The resulting pressure data are directly imported to the FEA simulation with interpolation to be used as a pressure load over the wing surface.

2.4. Wind Tunnel Experiments

The CFD analysis allows for a good prediction of aerodynamic coefficients but demands confirmation; this is accomplished through wind tunnel testing. The flying wing concept adopted may also pose a challenge from a stability viewpoint, and control surface tests can show whether each variant is stable. Additionally, in the Switchblade project, where advanced prototyping techniques are widely used, it is invaluable to test the airframe strength and stiffness, observing how it reacts to consistent forces provided in a wind tunnel setting.

The experiments were conducted in the National Wind Institute (NWI)'s closed-loop, subsonic wind tunnel at the Reese Technology Center. The test section is 1.2 m tall and 1.8 m wide, large enough to accommodate the aircraft half-model in its true scale, as shown in Figure 10a. The half-model is attached to a circular splitter plate and connected to an ATI 9150 Net Gamma 6-DoF load sensor with a resolution of 0.025 N for the lift and drag forces and 0.00125 N-m for the pitching moment. Figure 10b shows the center body, attached to

the load cell through slotted holes, which allows the UAV model to be installed in different longitudinal positions so the aerodynamic center can be identified. Figure 10c shows a schematic of the components of the system. The setup is also equipped with an Arduino microcontroller and servo for setting the elevon at different deflection angles.

2.4.1. Aerodynamic Center Finding Procedure

The aerodynamic center position was estimated analytically prior to wind tunnel testing; however, as seen in Figure 11, there is a great variation of the moment about that position with the angle of attack. Illustrated in Figure 10b are the slots used to move the model forward and back to determine the location of the aerodynamic center. By finding the point where the pitching moment remains constant as the angle of attack changes, the center is known. Although this was possible with the HSLR variant model, the limitations on the center body slots did not allow the exact placement of the aerodynamic center in the LSHE variant. In that case, the most forward position was used for all force and moment measurements.

2.4.2. Lift, Drag, and Moment Measurements

The objective of this experiment was to gather data on the lift and drag forces, as well as the pitching moment, which ideally should remain constant for the linear regime. The airspeed was set to each variant's cruise condition, with load cell data acquired using a National Instruments DAQ model 6353 with a sampling rate of 1000 Hz for a 30 s sample. The static angles of attack were set manually using a pitch link and a digital protractor with an error of $\pm 0.1^\circ$. The ranges of the angle of attack were from -2° to 17° for HSLR and from -2° to 14° for LSHE, with increments of 1° .

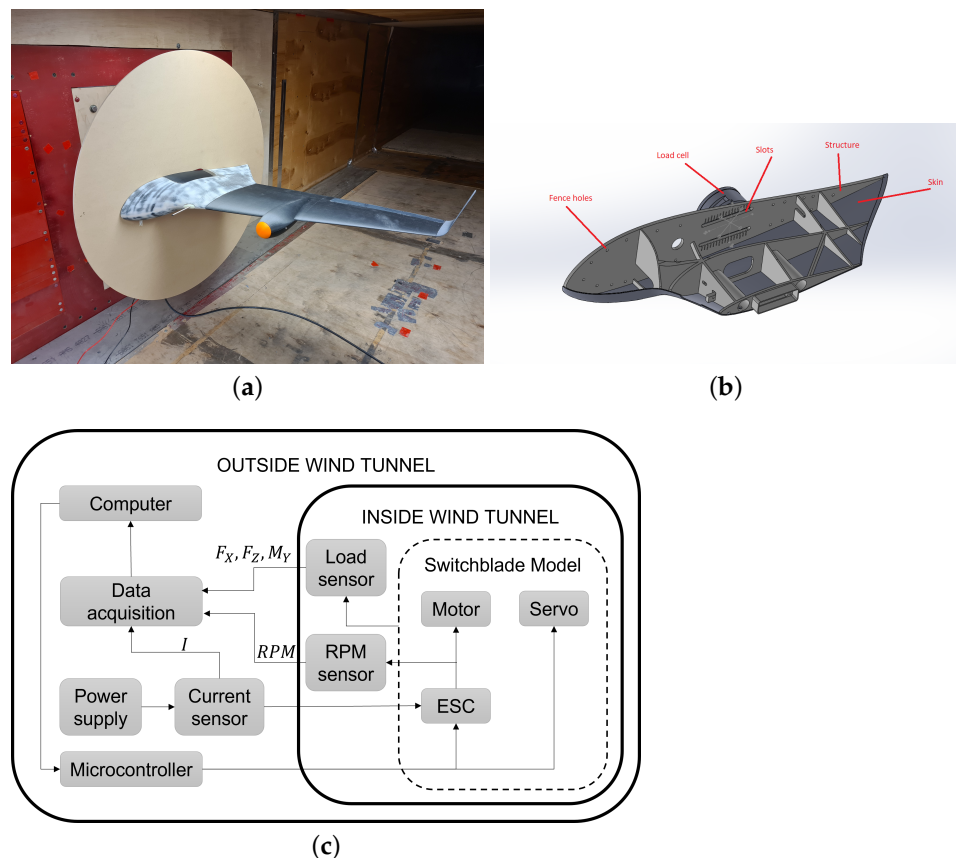


Figure 10. (a) Wind tunnel setup with HSLR variant; (b) wind tunnel center body; (c) experimental setup schematics.

2.4.3. Elevon Effectiveness and Trimming Procedure

Since Switchblade is a tailless aircraft, its neutral point location is the same as the aerodynamic center. This may have implications for stability and control that are better understood when running trimming experiments around the cruise condition for each variant. Ideally, there must not be a need for great control surface deflection to trim the tailless aircraft due to the reflex airfoils used. The experiments to find the cruise trim condition and necessary deflections on the wing control surface were required to evaluate its effectiveness. For these, the aircraft was fixed to the load cell at the longitudinal position that best approximated its aerodynamic center (hence, its neutral point) and commands were given to the wing-mounted servo to deflect the elevon at various angles to record the pitching moment coefficient.

2.4.4. Thrust Experiment

A thrust experiment was performed to compare the installed thrust with the available propeller performance data and to estimate the endurance and range for each variant. The propeller used was the APC 10 × 7 electric. For this experiment, measurements of the generated thrust, motor rotational speed, and free-stream velocity were recorded. As shown in Figure 10, the power supply is connected in series with a current sensor, which is then connected to the electronic speed controller (ESC) housed in the motor nacelle. The ESC receives signal input from an Arduino microcontroller outside the wind tunnel. The RPM sensor, connected to two phases of the motor, provides instant measurement of rotational speed, an important parameter for establishing the advance ratio $J = \frac{V_\infty}{n\phi}$, where V_∞ is the free-stream velocity, n is rotational speed, and ϕ is the propeller's diameter.

3. Results and Discussion

3.1. CFD Aerodynamic Results

In the first CFD simulations, the clean wing versions—LSHE and HSLR—were analyzed to obtain all aerodynamic coefficients and lift-to-drag L/D ratios, a direct measure of aerodynamic efficiency. Figure 11 shows the results for the clean wing versions of the aircraft. The lift coefficients show expected trends, where the LSHE has a lift-curve slope of 0.078, which is greater than the HSLR slope of 0.070. This difference in aspect ratio is associated with LSHE's having a slender wing with a smaller sweep. The stall angle of attack for the HSLR variant is approximately 11 degrees, with a very smooth stall behavior, as expected in low aspect ratio wings. Meanwhile, the LSHE variant shows an interesting behavior at $\alpha = 8^\circ$. The lift grows linearly up to that point, after which there is a sudden loss in the lift and recovery at $\alpha = 9^\circ$. Past this angle, the lift grows non-linearly, a trend shown in other aerodynamic coefficients; there is great increase in the drag generated for the LSHE variant and a drastic change in the pitching moment. The maximum L/D ratio is 19.68 for LSHE, at $\alpha = 6^\circ$ and 17.86 for HSLR, at $\alpha = 6^\circ$ as well. The base drag coefficient for both variants is very similar, approximately 0.014 for LSHE and 0.013 for HSLR.

To investigate the reason for the loss in lift seen in the low-speed variant, pressure fields were plotted for the clean wing at $\alpha = 8^\circ$, where the lift coefficient is still within the linear portion of the graph, and $\alpha = 9^\circ$ for comparison. The results are shown in Figure 12. The pressure plot shows that at the higher angle of attack, the pressure distribution at the interface between the wing panel and the center body becomes more homogeneous, increasing the pressure closer to the leading edge of the wing. Such a phenomenon is an indication that flow separation occurs in this condition, which is revealed in the turbulence plot shown in Figure 13.

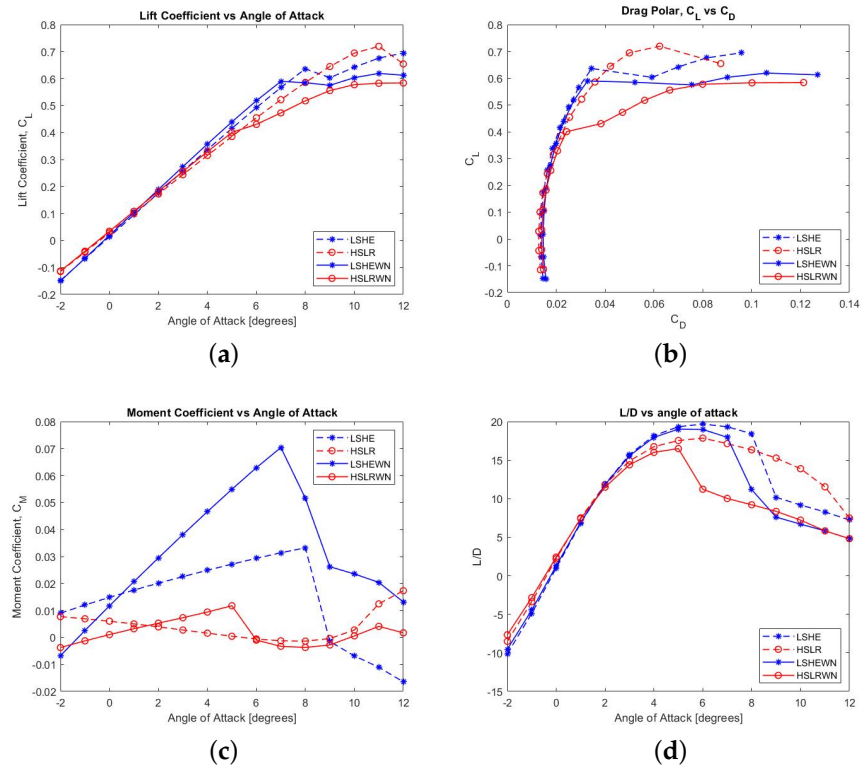


Figure 11. (a) C_L vs. α ; (b) drag polars; (c) C_M vs. α ; (d) L/D vs. α .

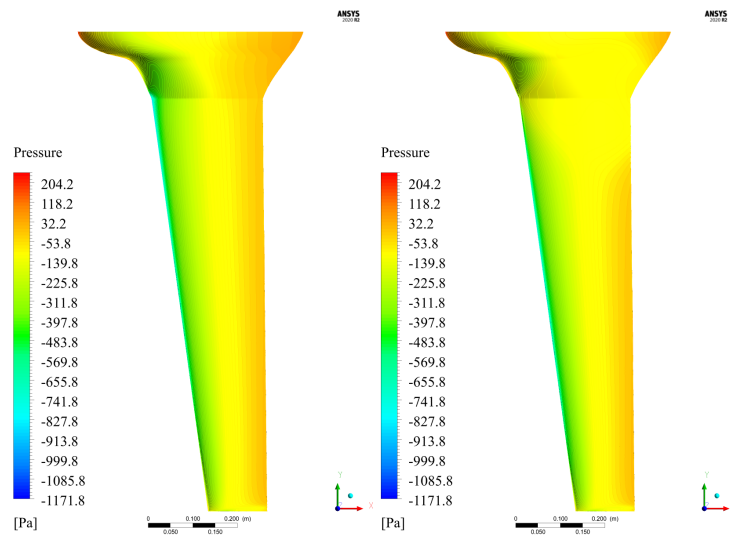


Figure 12. LSHE suction side pressure field comparison: left: $\alpha = 8^\circ$, right: $\alpha = 9^\circ$.

While at $\alpha = 8^\circ$, the turbulence intensity does not reach above approximately 3%. However, at $\alpha = 9^\circ$, it surpasses the 5% mark, indicating a highly turbulent state. This may be caused by the change in curvature between the center body and the wing at that location on the UAV.

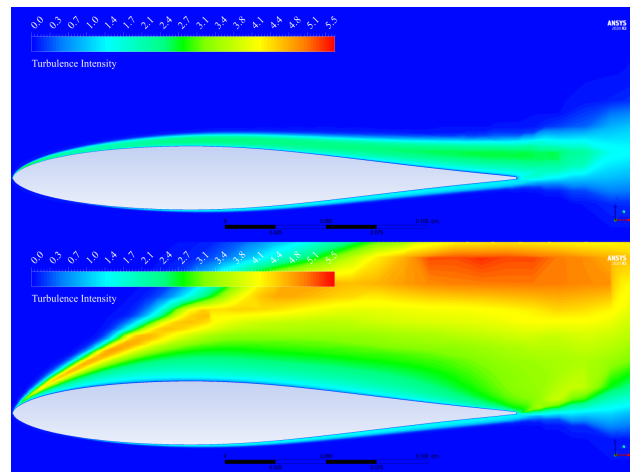


Figure 13. LSHE turbulence intensity at span location $y/b = 14\%$: top: $\alpha = 8^\circ$, bottom: $\alpha = 9^\circ$.

The second set of simulations involved analyzing the more detailed versions of the wings, those with winglets and motor nacelles. The nacelles are expected to add drag penalties to the aircraft, and it was uncertain whether the first winglet designs created during the conceptual design phase would provide a perceivable benefit in aerodynamic efficiency. The first simulations were run with the LSHEWN model, with the lowest cell count. The results show good agreement with the data previously obtained for the clean wing, achieving the same lift curve slope at the linear section of the graph and a similar lift decrease past that section. However, for the LSHEWN version, this drop in lift is smoother than what is observed for the LSHE.

The CFD analysis for the high-speed variant with winglet and nacelle revealed similar trends in the aerodynamic coefficients associated with flow separation facilitated by the nacelle. However, in this case, the change in lift generation was not as abrupt as seen in the low-speed variant. There is no decrease in lift coefficient value with the angle of attack, but, rather, a change in the lift curve's slope. These results are also shown in Figure 11. The drag coefficients and drag buckets of all wings are very similar up to $C_L = 0.4$. Then, there is a significant change in the drag, as seen in the drag polar. For the same lift coefficient, the drag on the HSLRWN wing is much higher than for the LSHEWN wing, due to the flow separating earlier on the former. These differences are reflected in the lift-to-drag ratios seen in both variants. While the maximum L/D for HSLRWN is approximately 16.5, at $\alpha = 5^\circ$, LSHEWN attains an L/D of 19.0, at $\alpha = 6^\circ$, or a 15.1% higher aerodynamic efficiency. The lift coefficients for the cruise condition for LSHE and HSLR are 0.412 and 0.204, respectively, which indicates that the LSHE variant operates very near its optimal point. The HSLR variant, however, is operating approximately at an L/D ratio of 12.5, which is 24.3% less than desired. Considering this, it is necessary to further reduce the wing dimensions and planform area accordingly. The pitch moment coefficients in Figure 11 show even greater differences between variants because the aerodynamic center location of the wing with the center body was uncertain, having been estimated with the simple graphic method [56]. The complex geometry of the center body, as well as the use of three different airfoils across the total span of the aircraft, makes it difficult to estimate the correct aerodynamic center location accurately. Wind tunnel experiments were used later to find this location.

Similar to the analysis performed on the clean wing low-speed geometry, pressure plots for the detailed wings were created to show what causes the changes in lift production on the top suction surface of the aircraft. Figure 14 presents those results. The low-speed variant shows a big region of homogeneous pressure around the motor nacelle at $\alpha = 9^\circ$. When comparing this pressure plot with Figure 12, it is suspected that the addition of the nacelle results in two separation regions: one associated with the wing center body's interface and the other associated with the nacelle alone. On the high-speed variant,

however, the pressure change region is much smaller at $\alpha = 6^\circ$. This difference may be due to the smaller aspect ratio of this wing, which produces flow re-circulation from the wing tips to reduce separation.

Figure 15 shows turbulence intensity plots at certain wing span locations where the pressure change is significant. They indicate that high turbulence occurs in the low-speed high-endurance aircraft, with values of 6% and 5% at $y/b = 14\%$ and $y/b = 43\%$, respectively. For the high-speed long-range aircraft, turbulence levels can reach 9%.

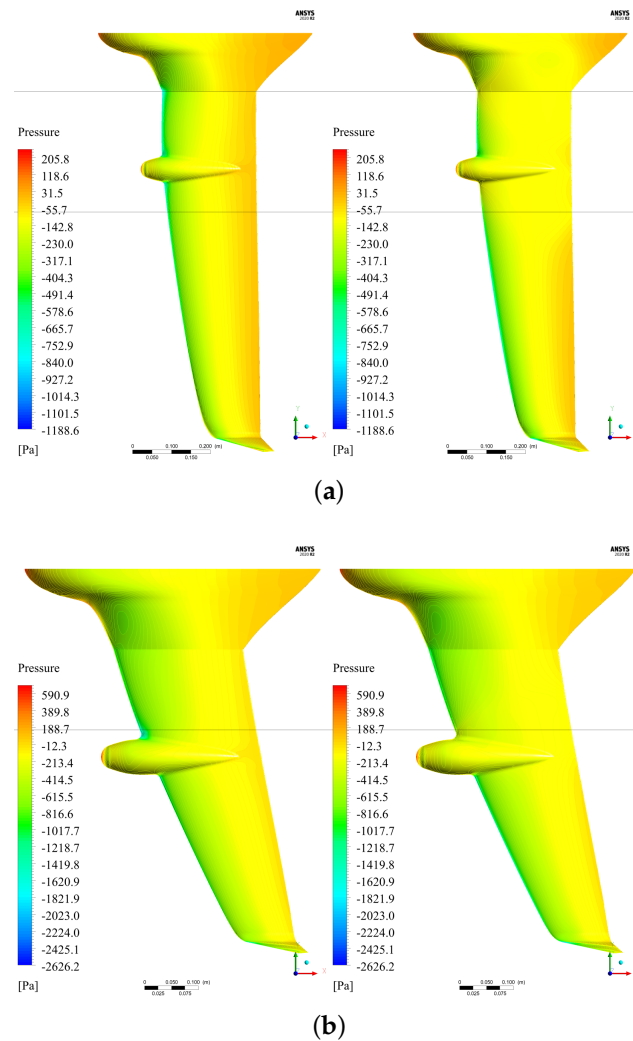


Figure 14. (a) LSHEWN suction side pressure field: left: $\alpha = 7^\circ$, right: $\alpha = 9^\circ$; (b) HSLRWN suction side pressure field: left: $\alpha = 5^\circ$, right: $\alpha = 6^\circ$.

Observing the CFD results, it is necessary to make further changes to the high-speed variant in order to operate near its maximum efficiency point. Flow separation occurring past the linear portion of the lift coefficient graphs was investigated further, using wind tunnel experiments to confirm the aerodynamic results and to determine if the flow behaviors are similar. The simulations did not include propeller downwash effects, which can have a very important role in energizing the flow, keeping it attached to the wing.

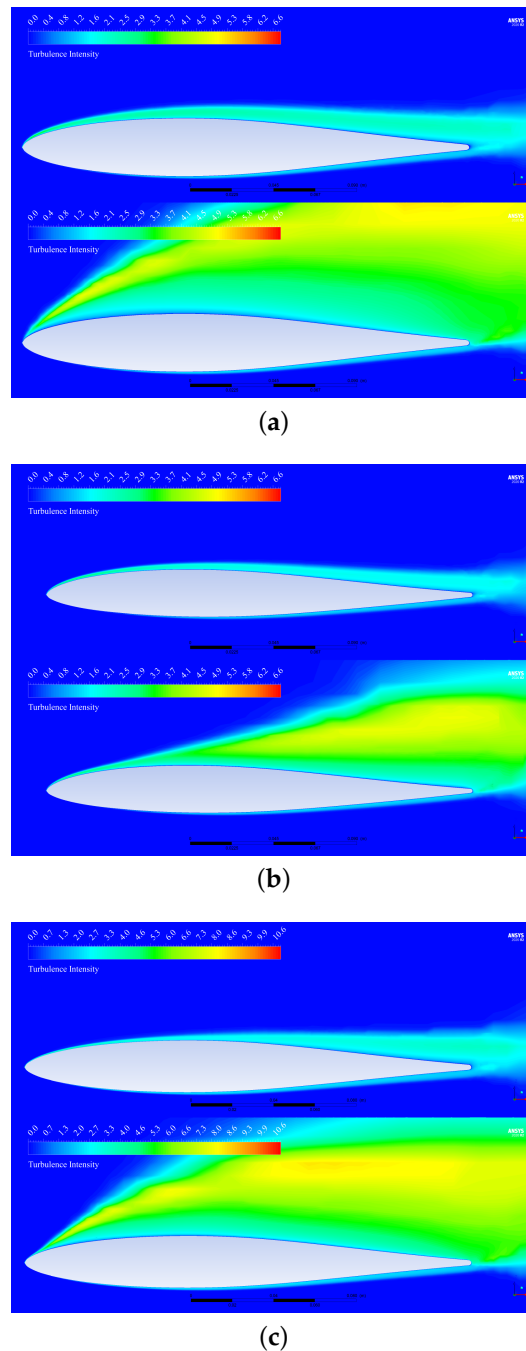


Figure 15. (a) LSHEWN turbulence intensity at $y/b = 14\%$: top: $\alpha = 7^\circ$, bottom: $\alpha = 9^\circ$; (b) LSHEWN turbulence intensity at $y/b = 43\%$: top: $\alpha = 7^\circ$, bottom: $\alpha = 9^\circ$; (c) HSLRWN turbulence intensity at $y/b = 42\%$: top: $\alpha = 5^\circ$, bottom: $\alpha = 6^\circ$.

3.2. FEA Results

The results were obtained for maximum load factor conditions: at corner speed with maximum C_L angle of attack, and for dive speed, or the highest speed that the aircraft should experience. Figures 16a,b show the factor of safety (FoS) plots for LSHE at corner speed and HSLR at dive speed, respectively. Computing factors of safety based on the Tsai–Wu failure criterion for each of the cases revealed that LSHE is very close to its strength limit in both conditions, with the FoS being 1.09 and 1.16 for the corner and dive speeds, respectively. The HSLR variant presents a much higher FoS due to its lower aspect ratio wing, despite the higher operating flight speeds. The FoS for that variant is 2.61 for corner speed and 2.48 for dive speed.

It was found that, in all of the load cases studied, the minimum factor of safety occurs in the same region of the aircraft, the front spar where it meets the nacelle. Due to its printing orientation, the internal structure is stiffer than the wing skin in the Y direction, which explains the higher stresses in the spar. In addition, the rounded nacelle contour in the spar acts as a stress concentration, contributing to peak stress at one of the sides of the nacelle. Figure 17 shows the plot of the stress component S_1 in the internal structure for LSHE corner speed and HSLR dive speed cases. The corresponding maximum stresses are summarized in Table 8. The maximum wing tip displacements, δ_{tip} , are 25.4 mm for the low-speed variant and 8.8 mm for the high-speed variant. The higher displacement on the low-speed aircraft was expected, given its greater wingspan, although higher speed operation would subject the aircraft to excessive deformation and stresses leading to a prohibitive factor of safety.

The reaction forces were computed to check the accuracy of the imported load in each case since it consists of the pressure data interpolated from the CFD mesh into the FEA mesh. These reaction forces can be converted into the lift being produced in the condition under analysis, as shown in Table 8. L_R is the lift calculated from the reaction forces R_X and R_Z , and L_{true} refers to the actual lift in the flight condition, calculated from aerodynamic coefficients in Figure 11. The reaction lift is 8.3% higher than the actual lift in the LSHE dive case, and 6.2% higher in the HSLR corner speed case.

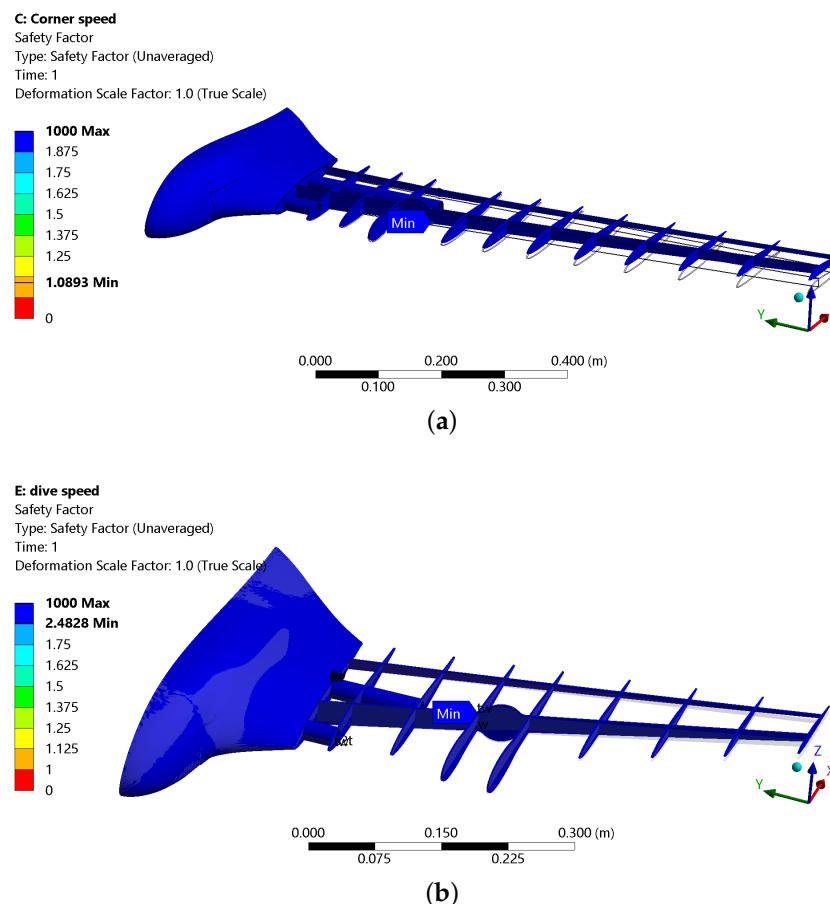
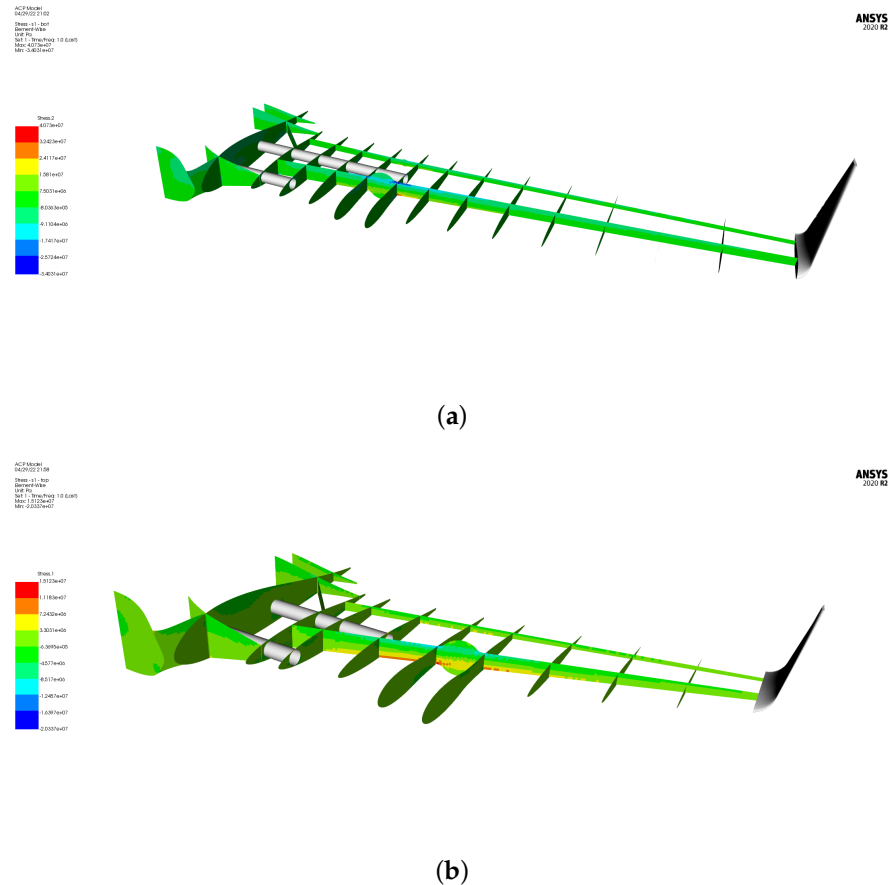


Figure 16. Factors of safety: (a) LSHE corner speed; (b) HSLR dive speed.

Table 8. FEA results summary.

Load Case	FoS	Spar $S_{1,max}$ [MPa]	δ_{tip} [mm]	R_X [N]	R_Z [N]	L_R [N]	L_{true} [N]
LSHE, corner	1.09	40.7	25.4	2.53	−65.51	129.6	132.4
LSHE, dive	1.16	38.2	24.2	5.05	−71.57	143.4	132.4
HSLR, corner	2.61	14.3	8.3	2.60	−70.50	139.0	130.8
HSLR, dive	2.48	15.1	8.8	1.40	−65.58	131.1	130.8

**Figure 17.** Internal structure S1 stress component: (a) LSHE, corner speed; (b) HSLR, dive speed.

3.3. Experimental Results

The aerodynamic results are shown in Figure 18. The lift coefficient curves in (a) indicate the LSHE variant produces more lift than its counterpart. The maximum lift coefficient, C_{Lmax} for this variant is 0.97, at $\alpha = 13^\circ$, whereas, for the HSLR variant, it is 0.91, at $\alpha = 14^\circ$, a 6.1% smaller C_{Lmax} . The design lift coefficients for cruise speed on HSLR is 0.21, at an angle of attack of $\alpha = 2.0^\circ$, while, on LSHE, it is 0.42, at $\alpha = 4.0^\circ$. The difference in the shapes of the lift coefficient curves is in accordance with wings that have different aspect ratios, with the lower aspect ratio HSLR variant having a smoother stall region, as well as a higher stall angle of attack.

The drag polars in Figure 18b show that both variants produce similar drags up to $C_L = 0.48$. For a higher C_L , where induced drag effects predominate, the LSHE variant produces less drag due to its higher aspect ratio. The base drag coefficients for LSHE and HSLR are 0.016 and 0.015, respectively. The lift-to-drag ratio curves in Figure 18c indicate the LSHE variant has a maximum L/D of 18.2, or 12.6% higher than HSLR, with an $L/D = 16.2$. At its cruise speed, LSHE operates with an $L/D = 15.9$, which is 29.9% more aerodynamically efficient than HSLR at its cruise speed, with an $L/D = 12.3$. Due to its higher cruise speed, the high-speed variant operates further from its maximum L/D , around 24.2% less than optimal, which indicates the aircraft should have its wing

area reduced accordingly. The low-speed variant operates closer to the maximum L/D , although 12.5% less than optimal.

The pitching moment coefficients are shown in Figure 18d. For the HSLR variant, it does not change considerably with angle of attack for the linear range in the lift curve. Past $\alpha = 13^\circ$, C_M decreases abruptly due to stall propagation effects throughout the wing. This behavior shows the aircraft pitches down during stall, which is a desirable tendency. The LSHE variant presents considerable change in C_M with angle of attack due to the point of measurement lying behind the aerodynamic center of the aircraft. This is demonstrated by the positive slope of the C_M vs. α curve.

When comparing the experimental and computational results at cruise angles of attack, HSLR and LSHE produce a 26.9% and 18.8% higher C_L than predicted with CFD. This difference increases at higher angles, with the C_L for HSLR and LSHE being 52.6% and 57.7% higher at $\alpha = 12^\circ$. The drag coefficient remains very similar at the lower C_L region of Figure 18b, with HSLR showing a 19.0% higher C_D than the CFD results at cruise conditions, whereas the LSHE experimental results show a 33.6% higher drag. Above $C_L = 0.4$ for HSLR and approximately 0.6 for LSHE, the drag from the experiments is much smaller, since the early separation shown in the CFD model does not occur. This causes the lift-to-drag ratio of the variants to diverge past $\alpha = 5^\circ$ (HSLR) and 7° (LSHE).

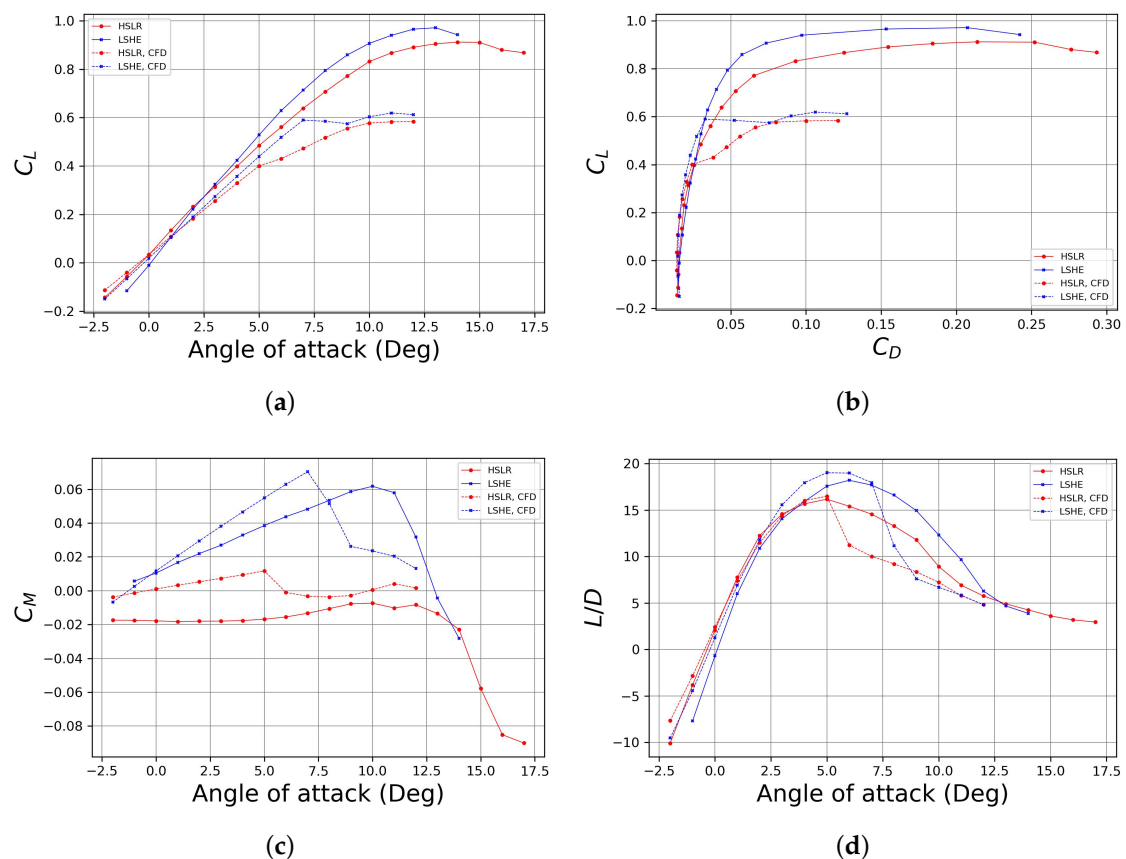


Figure 18. Experimental results. (a) C_L vs. α ; (b) Drag polars; (c) C_M vs. α ; (d) L/D vs. α .

The experimental aerodynamic coefficients show a considerable difference from the CFD results, which can be attributed to the challenges in modeling turbulence accurately—particularly in transitional flow. The reduction in the lift slope predicted from CFD is not present in the experimental data, which points to the $k-\omega$ SST model's tendency to over-predict flow separation regions [57]. The inlet boundary condition assumptions and flow domain size in the CFD analysis also contribute to the difference in results. The decay of turbulence from the inlet to the aircraft results in very low turbulence intensity at the free stream close to the

aircraft, as opposed to real conditions experienced in the wind tunnel [58]. The CFD incoming flow, as shown in Figures 13 and 15, is perfectly laminar upon reaching the aircraft geometry, while recent measurements from a different work have shown that the streamwise turbulence intensity at the center of the test section is 1.2% at an average flow velocity of 10.85 m/s [59]. Higher-than-expected turbulence intensity delays flow separation in the wind tunnel model, leading to higher lift coefficients for both variants and separation phenomena of different behaviors from the CFD results. Wind tunnel experiments on a 2-D wind turbine blade have shown that higher inlet turbulence intensity can result in a lift increase of up to 46.2% [60], suggesting that this effect is at play in the wind tunnel tests, in combination with the increased 3-D effects from the finite wings, leading to a higher C_L and C_D .

The control surface effectiveness in trimming is shown in Figure 19. The elevon deflection angle is defined as positive for a pitch-up attitude. For the HSLR variant, the elevon is capable of trimming the aircraft with a deflection of $\delta_e = 3^\circ$, and it can provide a wide range of C_M , from approximately -0.10 at $\delta_e = -19^\circ$ to 0.08 at $\delta_e = 25^\circ$. For the LSHE variant, since its neutral point could not be found, a positive pitching moment exists at $\delta_e = 0$. Trimming the aircraft in this condition would require a deflection of $\delta_e = -2.4^\circ$. The elevon is capable of providing a minimum C_M of -0.03 , which is not as low as with the HSLR variant. However, it is believed that the pitch-down moment would be higher if measured at the adequate location. In future experiments, the center body must be altered to allow more travel for load cell adjustment.

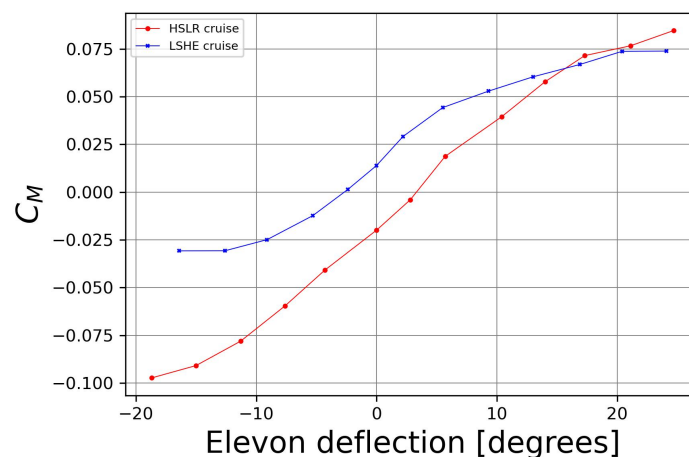


Figure 19. Pitching moment coefficient vs. elevon deflection.

The thrust experiment shows that the installed thrust is lower than available data measured for the same propeller in [61], with the difference being up to 23% at $J = 0.6$. The results are shown in Figure 20. Assuming the difference in thrust is due to installation effects and the wind tunnel environment, the experimental data were used as a starting point for propeller efficiency estimates. Due to limitations in the setup, higher advance ratios were not tested. To evaluate the installed thrust at higher advance ratios, C_T was considered to be 23% lower than the available data. An extensive experimental database on small propellers is found in [62].

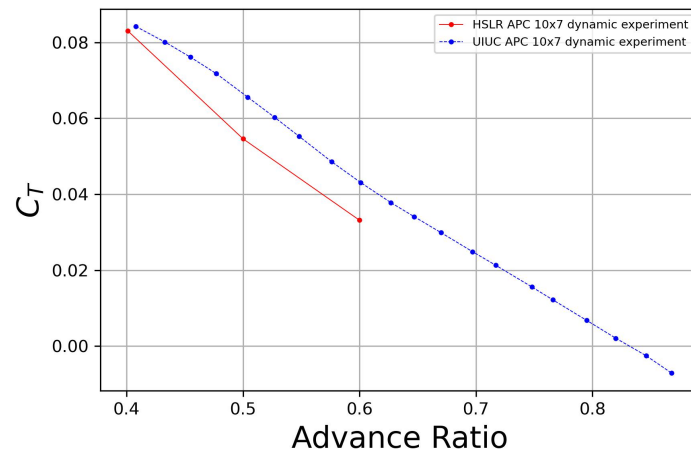


Figure 20. Thrust coefficient vs. advance ratio, comparison with available data [62].

At cruise, the thrust coefficient required from the aircraft and the advance ratio are given by

$$C_T = \frac{D}{\rho n^2 \phi^4} \quad (7)$$

$$J = \frac{V_\infty}{n\phi} \quad (8)$$

substituting the advance ratio into C_T and writing the drag as a coefficient lead to

$$C_T = \frac{C_D S J^2}{\phi^2} \quad (9)$$

Using this equation is an iterative process, since choosing a value for the advance ratio, J , allows for the calculation of the thrust coefficient at cruise but not necessarily will C_T match the real performance of the propeller at such advance ratio. Moreover, each Switchblade variant has a different cruise drag, wing area, and advance ratio due to different cruise speeds, which will result in different propeller efficiencies η_p . Using this equation for HSLR, $J = 0.74$ and $C_T = 0.013$; for LSHE, $J = 0.68$ and $C_T = 0.023$. Propeller efficiencies at those conditions are 58% and 68%, respectively.

The aircraft performance was evaluated in terms of the endurance and range for both variants by using the equation for electric propulsion derived in [63]:

$$E = R_t^{1-m} \left[\frac{\eta_{tot} VC}{\frac{1}{2} \rho V_\infty^3 S C_{D0} + (2W^2 k / \rho V_\infty S)} \right]^m \quad (10)$$

where E is the endurance in hours, R_t is the battery hour rating, m is a discharge parameter, and η_{tot} is the total efficiency of the propulsion system. V is the voltage, and C is the battery capacity in Ampere-hour, where a capacity of 10 Ampere-hours is used on the Switchblade calculations. On the bottom of the equation, aircraft parameters are used, such as base drag C_{D0} , weight W , and the slope of the drag polar at cruise condition, k . The results from Equation (10) are shown in Table 9.

Table 9. Endurance and range by variant.

Variant	Flight Speed [m/s]	Endurance [h]	Range [km]
LSHE	20.16	1.80	131
HSLR	33.62	0.49	59

The low-speed high-endurance variant has an endurance of 1.8 h, enabling it to attain a range of 131 km. The high-speed long-range aircraft has a reduced endurance due to its lower propeller efficiency and suboptimal L/D ratio at cruise. At a higher speed, the power drawn from the battery is higher, thus reducing the operating time. In this case, the endurance and range are 0.49 h and 59 km. Despite the lower endurance, the HSLR variant is capable of operating outside of the flight envelope of the LSHE, as shown previously in Figure 9. This signifies that it can sustain a 66.7% higher cruise speed for time-critical tasks without exceeding the load limits established in the maneuver diagram. Additionally, to obtain a better performance from a higher speed flight, the HSLR variant must be further modified to bring its operating point closer to the maximum L/D ratio. This can be attained by resizing its wing, causing it to fly at higher angles of attack, and, therefore, at higher efficiency.

4. Conclusions

This paper presents a multidisciplinary analysis of a reconfigurable UAV intended for multiple missions, consisting of computational design, numerical simulations in CFD and FEA, and wind tunnel experiments for validation. Previous studies by the authors have indicated, on a conceptual level, that reconfigurable unmanned aircraft have the potential to disrupt the UAV industry by offering significant cost reduction and supply chain benefits due to fewer airframe parts. These benefits increase with the number of UAV variants in the system, however, design challenges and performance trade-offs become more numerous. Designing each variant to operate in cruise at its peak aerodynamic efficiency was shown to be challenging to achieve, in part due to the complex aerodynamics of the blended wing body, which is difficult to model analytically prior to CFD analysis.

Both the CFD and the experimental results revealed that the low-speed high-endurance Switchblade variant operates off-optimally aerodynamically, and the high-speed long-range variant especially would benefit from a design iteration to adjust its wing geometry and reduce planform area. The CFD underestimated lift for most of the angles of attack examined and overestimated the drag for higher angles due to flow separation effects that are not indicated in the wind tunnel experimental results. Control surface effectiveness was also evaluated via experimental testing, showing that both variants can be trimmed for cruise flight. Propulsion experiments provided an estimate of how much the installed thrust differs from propeller data, serving as a basis to calculate endurance and range for both Switchblade variants. The low-speed high-endurance (LSHE) aircraft has an estimated flight endurance of 1 h and 48 min, with a maximum range of 131 km. The high-speed long-range (HSLR) variant shows an endurance and range of approximately one half-hour and 59 km, respectively. Although this variant operates off-optimally, it is able to sustain speeds beyond the flight envelope of its counterpart safely. Further design improvements can cause both variants to operate at maximum efficiency.

In the finite element studies, the 3-D printing material Nylon 12 CF was modeled with orthotropic properties, and the Tsai–Wu failure criterion for composites was used. The simulation showed that the HSLR variant operates safely in both critical loading conditions, namely corner speed and dive speed, with factors of safety (FoS) of 2.61 and 2.48, respectively; in the same flight conditions, the LSHE variant operates with lower FoS, 1.09 and 1.16. This indicates that improvements in the airframe are necessary to account for the higher aspect ratio of that variant.

Moreover, the research sheds light on the design challenge of modular aircraft for optimal performance, exploring high-order computational methods for the analysis of a concept from product platform planning. A similar approach can be applied to other vehicles or products that benefit from rapid prototyping and multiple combinations for distinct performance. Some examples are planetary rovers and habitats, electrical and urban mobility vehicles, medical prostheses, and wind turbines. The research revealed some limitations in accurately modeling flow separation on a 3-D blended wing body using CFD, as evidenced by its over-prediction in comparison with experimental results.

This, combined with the challenge of modeling the blended wing body analytically in the conceptual phase, opens room for improvement in future studies. It is recommended that the conceptual design framework be served by more sophisticated techniques, such as the vortex lattice method (VLM) or a surface vorticity flow solver. These tools, although still low-order, would be able to provide a better starting point for a combined high-order computational analysis. Another possibility would be to add a structural aspect to the wind tunnel experiments, to provide the structural design discipline with an extra source of correction. Future studies will focus on understanding the unsteady aerodynamics and stall of the UAV under dynamic pitch oscillations using load sensing and particle image velocimetry (PIV) techniques.

Author Contributions: Conceptualization, D.S. and V.M.; methodology, D.S. and J.R.; software, J.R.; validation, D.S., J.R. and A.D.R.; formal analysis, J.R. and A.D.R.; investigation, D.S.; resources, A.D.R.; data curation, A.D.R.; writing—original draft preparation, D.S., A.D.R. and J.R.; writing—review and editing, V.M.; visualization, D.S.; supervision, V.M.; project administration, V.M. and D.S.; funding acquisition, V.M. The authors have contributed equally to all sections and tasks. All authors have read and agreed to the published version of the manuscript.

Funding: This work was supported by the Department of Mechanical Engineering, Texas Tech University, as part of the startup package of Victor Maldonado.

Data Availability Statement: Data will be provided upon request.

Acknowledgments: The authors would like to acknowledge David Myers for his indispensable experience and help in manufacturing the experimental setup used in this work. Without him, most of the experiments would not have been possible.

Conflicts of Interest: The authors declare no conflict of interest.

Abbreviations

The following abbreviations are used in this manuscript:

UAV	Unmanned Aerial Vehicle
UAS	Unmanned Aerial System
CFD	Computational Fluid Dynamics
RANS	Reynolds-Averaged Navier–Stokes
URANS	Unsteady Reynolds-Averaged Navier–Stokes
DES	Detached Eddy Simulation
FEA	Finite Element Analysis
RVE	Representative Volume Element
HSLR	High-Speed Long-Range
LSHE	Low-Speed High-Endurance
AoA	Angle-of-Attack
DoF	Degrees of Freedom

References

1. Goh, C.Y.; Leow, C.Y.; Nordin, R. Energy Efficiency of Unmanned Aerial Vehicle with Reconfigurable Intelligent Surfaces: A Comparative Study. *Drones* **2023**, *7*, 98. [[CrossRef](#)]
2. Yang, Z.; Yu, X.; Dedman, S.; Rosso, M.; Zhu, J.; Yang, J.; Xia, Y.; Tian, Y.; Zhang, G.; Wang, J. UAV remote sensing applications in marine monitoring: Knowledge visualization and review. *Sci. Total. Environ.* **2022**, *838*, 155939. [[CrossRef](#)]
3. Mozaffari, M.; Saad, W.; Bennis, M.; Nam, Y.H.; Debbah, M. A Tutorial on UAVs for Wireless Networks: Applications, Challenges, and Open Problems. *IEEE Commun. Surv. Tutor.* **2019**, *21*, 2334–2360. [[CrossRef](#)]
4. Zhao, C.; Shi, K.; Tang, Y.; Xiao, J.; He, N. Multi-Group Tracking Control for MASs of UAV with a Novel Event-Triggered Scheme. *Drones* **2023**, *7*, 474. [[CrossRef](#)]
5. Lyu, M.; Zhao, Y.; Huang, C.; Huang, H. Unmanned Aerial Vehicles for Search and Rescue: A Survey. *Remote. Sens.* **2023**, *15*, 3266. [[CrossRef](#)]
6. Hu, P.; Zhang, R.; Yang, J.; Chen, L. Development Status and Key Technologies of Plant Protection UAVs in China: A Review. *Drones* **2022**, *6*, 354. [[CrossRef](#)]

7. Kaitao, M.; Wu, Q.; Xu, J.; Chen, W.; Feng, Z.; Schober, R.; Swindlehurst, A. UAV-Enabled Integrated Sensing and Communication: Opportunities and Challenges. *IEEE Wirel. Commun.* **2023**, 1–9. [\[CrossRef\]](#)
8. Su, J.; Zhu, X.; Li, S.; Chen, W.H. AI meets UAVs: A survey on AI empowered UAV perception systems for precision agriculture. *Neurocomputing* **2023**, *518*, 242–270. [\[CrossRef\]](#)
9. da Silva, Ferreira, M.A.; Begazo, M.F.T.; Lopes, G.C.; de Oliveira, A.F.; Colombini, E.L.; da Silva, Simões, A. Drone Reconfigurable Architecture (DRA): A Multipurpose Modular Architecture for Unmanned Aerial Vehicles (UAVs). *J. Intell. Robot. Syst.* **2020**, *99*, 517–534. [\[CrossRef\]](#)
10. Chowdhury, S.; Maldonado, V.; Tong, W.; Messac, A. New Modular Product-Platform-Planning Approach to Design Macroscale Reconfigurable Unmanned Aerial Vehicles. *J. Aircr.* **2016**, *53*, 309–322. [\[CrossRef\]](#)
11. Pate, D.J.; Patterson, M.D.; German, B.J. Optimizing Families of Reconfigurable Aircraft for Multiple Missions. *J. Aircr.* **2012**, *49*, 1988–2000. [\[CrossRef\]](#)
12. Maldonado, V.; Santos, D.; Wilt, M.; Ramirez, D.; Shoemaker, J.; Ayele, W.; Beeson, B.; Lisby, B.; Zamora, J.; Antu, C. ‘Switchblade’: Wide-Mission Performance Design of a Multi-Variant Unmanned Aerial System. In Proceedings of the AIAA Scitech 2021 Forum, Virtual Event, 11–15 January 2021. [\[CrossRef\]](#)
13. Santos, D.; Ramirez, D.; Rogers, J.; Zamora, J.; Rezende, A.; Maldonado, V. Full-Cycle Design and Analysis of the Switchblade Reconfigurable Unmanned Aerial System. In Proceedings of the AIAA Aviation 2022 Forum, Chicago, IL, USA, 27 June–1 July 2022. [\[CrossRef\]](#)
14. El Adawy, M.; Abdelhalim, E.H.; Mahmoud, M.; Ahmed Abo zeid, M.; Mohamed, I.H.; Othman, M.M.; ElGamal, G.S.; ElShabasy, Y.H. Design and fabrication of a fixed-wing Unmanned Aerial Vehicle (UAV). *Ain Shams Eng. J.* **2023**, *14*, 102094. [\[CrossRef\]](#)
15. Ayele, W.; Maldonado, V. Conceptual Design of a Robotic Ground-Aerial Vehicle with an Aeroelastic Wing Model for Mars Planetary Exploration. *Aerospace* **2023**, *10*, 404. [\[CrossRef\]](#)
16. Chu, L.; Gu, F.; Du, X.; He, Y. Design and analysis of morphing wing UAV adopted to harsh environment based on “Frigate bird”. In Proceedings of the 2022 IEEE International Conference on Robotics and Biomimetics (ROBIO), Jinghong, China, 5–9 December 2022; pp. 1295–1300. [\[CrossRef\]](#)
17. Elelwi, M.; Kuitche, M.; Botez, R.; Dao, T. Comparison and analyses of a variable span-morphing of the tapered wing with a varying sweep angle. *Aeronaut. J.* **2020**, *124*, 1146–1169. [\[CrossRef\]](#)
18. Gatto, A. Development of a morphing UAV for optimal multi-segment mission performance. *Aeronaut. J.* **2023**, *127*, 1320–1352. [\[CrossRef\]](#)
19. Goetzendorf-Grabowski, T.; Tarnowski, A.; Figat, M.; Mieloszyk, J.; Hernik, B. Lightweight unmanned aerial vehicle for emergency medical service—Synthesis of the layout. *Proc. Inst. Mech. Eng. Part J. Aerosp. Eng.* **2021**, *235*, 5–21. [\[CrossRef\]](#)
20. Kim, T.; Jeaong, H.; Kim, S.; Kim, I.; Kim, S.; Suk, J.; Shin, H.S. Design and Flight Testing of the Ducted-fan UAV Flight Array System. *J. Intelligent Robot. Syst.* **2023**, *107*. [\[CrossRef\]](#)
21. Lu, D.; Xiong, C.; Zhou, H.; Lyu, C.; Hu, R.; Yu, C.; Zeng, Z.; Lian, L. Design, fabrication, and characterization of a multimodal hybrid aerial underwater vehicle. *Ocean. Eng.* **2021**, *219*, 108324. [\[CrossRef\]](#)
22. Lyu, C.; Lu, D.; Xiong, C.; Hu, R.; Jin, Y.; Wang, J.; Zeng, Z.; Lian, L. Toward a gliding hybrid aerial underwater vehicle: Design, fabrication, and experiments. *J. Field Robot.* **2022**, *39*, 543–556. [\[CrossRef\]](#)
23. Savastano, E.; Perez-Sanchez, V.; Arrue, B.; Ollero, A. High-Performance Morphing Wing for Large-Scale Bio-Inspired Unmanned Aerial Vehicles. *IEEE Robot. Autom. Lett.* **2022**, *7*, 8076–8083. [\[CrossRef\]](#)
24. Wong, S.M.; Ho, H.W.; Abdullah, M.Z. Design and Fabrication of a Dual Rotor-Embedded Wing Vertical Take-Off and Landing Unmanned Aerial Vehicle. *Unmanned Syst.* **2021**, *9*, 45–63. [\[CrossRef\]](#)
25. Wang, Y.C.; Chen, T.; Yeh, Y.L. Advanced 3D printing technologies for the aircraft industry: A fuzzy systematic approach for assessing the critical factors. *Int. J. Adv. Manuf. Technol.* **2019**, *105*, 4059–4069. [\[CrossRef\]](#)
26. Liu, X.; Li, D.; Qi, P.; Qiao, W.; Shang, Y.; Jiao, Z. A local resistance coefficient model of aircraft hydraulics bent pipe using laser powder bed fusion additive manufacturing. *Exp. Therm. Fluid Sci.* **2023**, *147*, 110961. [\[CrossRef\]](#)
27. Kobenko, S.; Dejus, D.; Jātnieks, J.; Pazars, D.; Glaskova-Kuzmina, T. Structural Integrity of the Aircraft Interior Spare Parts Produced by Additive Manufacturing. *Polymers* **2022**, *14*, 1538. [\[CrossRef\]](#) [\[PubMed\]](#)
28. Zhu, W. Models for wind tunnel tests based on additive manufacturing technology. *Prog. Aerosp. Sci.* **2019**, *110*, 100541. [\[CrossRef\]](#)
29. Raza, A.; Farhan, S.; Nasir, S.; Salamat, S. Applicability of 3D Printed Fighter Aircraft Model for Subsonic Wind Tunnel. In Proceedings of the 2021 International Bhurban Conference on Applied Sciences and Technologies (IBCAST), Islamabad, Pakistan, 12–16 January 2021; pp. 730–735. [\[CrossRef\]](#)
30. Bardera, R.; Ángel Rodríguez-Sevillano.; Barderas, E.B.; Casati, M.J., Rapid prototyping by additive manufacturing of a bioinspired micro-RPA morphing model for a wind tunnel test campaign. In Proceedings of the AIAA AVIATION 2022 Forum, Chicago, IL, USA, 27 June–1 July 2022. [\[CrossRef\]](#)
31. Tsushima, N.; Saitoh, K.; Nakakita, K. Structural and aeroelastic characteristics of wing model for transonic flutter wind tunnel test fabricated by additive manufacturing with AlSi10Mg alloys. *Aerosp. Sci. Technol.* **2023**, *140*, 108476. [\[CrossRef\]](#)
32. Taylor, R.M.; Niakin, B.; Lira, N.; Sabine, G.; Lee, J.; Conklin, C.; Advirkar, S. Design Optimization, Fabrication, and Testing of a 3D Printed Aircraft Structure Using Fused Deposition Modeling. In Proceedings of the AIAA Scitech 2020 Forum, Orlando, FL, USA, 6–10 January 2020. [\[CrossRef\]](#)

33. Skawinski, I.; Goetzendorf-Grabowski, T. FDM 3D printing method utility assessment in small RC aircraft design. *Aircr. Eng. Aerosp. Technol.* **2019**, *91*, 865–872. [[CrossRef](#)]
34. Mani, M.; Dorgan, A.J. A Perspective on the State of Aerospace Computational Fluid Dynamics Technology. *Annu. Rev. Fluid Mech.* **2023**, *55*, 431–457. [[CrossRef](#)]
35. Ma, Z.; Tang, Z.; Wang, R.; Yu, Z. Research Progress in Numerical Simulation of Aircraft Wing Flow Field. *J. Phys. Conf. Ser.* **2023**, *2457*, 012047. [[CrossRef](#)]
36. Le Clainche, S.; Ferrer, E.; Gibson, S.; Cross, E.; Parente, A.; Vinuesa, R. Improving aircraft performance using machine learning: A review. *Aerosp. Sci. Technol.* **2023**, *138*, 108354. [[CrossRef](#)]
37. García-Gutiérrez, A.; Gonzalo, J.; López, D.; Delgado, A. Advances in CFD Modeling of Urban Wind Applied to Aerial Mobility. *Fluids* **2022**, *7*, 246. [[CrossRef](#)]
38. Panagiotou, P.; Yakinthos, K. Aerodynamic efficiency and performance enhancement of fixed-wing UAVs. *Aerosp. Sci. Technol.* **2020**, *99*, 105575. [[CrossRef](#)]
39. Tormalm, M.; Schmidt, S. Computational Study of Static And Dynamic Vortical Flow over the Delta Wing SACCON Configuration Using the FOI Flow Solver Edge. In Proceedings of the 28th AIAA Applied Aerodynamics Conference, Chicago, IL, USA, 28 June–1 July 2010. [[CrossRef](#)]
40. Sandoval, P.; Cornejo, P.; Tinapp, F. Evaluating the longitudinal stability of an UAV using a CFD-6DOF model. *Aerosp. Sci. Technol.* **2015**, *43*, 463–470. [[CrossRef](#)]
41. Mumtaz, M.S.; Maqsood, A.; Sherbaz, S. Computational Modeling of Dynamic Stability Derivatives for Generic Airfoils. *MATEC Web Conf.* **2017**, *95*, 12006. [[CrossRef](#)]
42. Greenblatt, D.; Williams, D.R. Flow Control for Unmanned Air Vehicles. *Annu. Rev. Fluid Mech.* **2022**, *54*, 383–412. [[CrossRef](#)]
43. Kim, M.; Kim, S.; Kim, W.; Kim, C.; Kim, Y. Flow Control of Tiltrotor Unamned-Aerial-Vehicle Airfoils Using Synthetic Jets. *J. Aircr.* **2011**, *48*, 1045–1057. [[CrossRef](#)]
44. Bliamis, C.; Vlahostergios, Z.; Misirlis, D.; Yakinthos, K. Numerical Evaluation of Riblet Drag Reduction on a MALE UAV. *Aerospace* **2022**, *9*, 218. [[CrossRef](#)]
45. Guiler, R.; Huebsch, W. Wind Tunnel Analysis of a Morphing Swept Wing Tailless Aircraft. In Proceedings of the 23rd AIAA Applied Aerodynamics Conference, Toronto, ON, Canada, 6–9 June 2005. [[CrossRef](#)]
46. Goetten, F.; Finger, D.; Marino, M.; Bil, C.; Havermann, M.; Braun, C. A Review of Guidelines and Best Practices for Subsonic Aerodynamic Simulations Using RANS CFD. In Proceedings of the Asia Pacific International Symposium on Aerospace Technology, Gold Coast, Australia, 4–6 December 2019.
47. Zore, K.; Shah, S.; Stokes, J.; Sasanapuri, B.; Sharkey, P. ANSYS CFD Study for High Lift Aircraft Configurations. In Proceedings of the 2018 Applied Aerodynamics Conference, Atlanta, GA, USA, 25–29 June 2018. [[CrossRef](#)]
48. Menter, F.R.; Smirnov, P.E.; Liu, T.; Avancha, R. A One-Equation Local Correlation-Based Transition Model. *Flow Turbul. Combust* **2015**, *95*, 583–619. [[CrossRef](#)]
49. Menter, F. Two-Equation Eddy-Viscosity Turbulence Models for Engineering Applications. *AIAA J.* **1994**, *32*, 8. [[CrossRef](#)]
50. Vostruha, K.; Pelant, J. Perturbation Analysis of “ $k - \omega$ ” and “ $k - \epsilon$ ” Turbulent Models. Wall Functions. *EPJ Web Conf.* **2013**, *45*, 01097. [[CrossRef](#)]
51. Rodriguez, S. *Applied Computational Fluid Dynamics and Turbulence Modeling: Practical Tools, Tips and Techniques*; Springer International Publishing: Berlin/Heidelberg, Germany, 2019.
52. Gu, J.; Chen, P.; Su, L.; Li, K. A theoretical and experimental assessment of 3D macroscopic failure criteria for predicting pure inter-fiber fracture of transversely isotropic UD composites. *Compos. Struct.* **2020**, *259*, 113466.
53. Stratasys. Nylon 12 Carbon Fiber, 2015. Available online: <https://www.stratasys.com/en/materials/materials-catalog/fdm-materials/Nylon-12/> (accessed on 6 June 2022).
54. Chen, R.; Ramachandran, A.; Liu, C.; Chang, F.K.; Senesky, D. Tsai-Wu Analysis of a Thin-Walled 3D-Printed Polylactic Acid (PLA) Structural Bracket. In Proceedings of the 58th AIAA/ASCE/AHS/ASC Structures, Structural Dynamics, and Materials Conference, Grapevine, TX, USA, 9–13 January 2017. [[CrossRef](#)]
55. Administration, F.A. Federal Aviation Regulations Part 23, § 23.337, 2023. Available online: <https://www.govinfo.gov/app/details/CFR-2017-title14-vol1/CFR-2017-title14-vol1-sec23-337> (accessed on May 4, 2022).
56. Raymer, D. *Aircraft Design: A Conceptual Approach*; American Institute of Aeronautics and Astronautics: Reston, VA, USA, 2012; pp. 203–205. [[CrossRef](#)]
57. Evans, S.; Lardeau, S. Validation of a turbulence methodology using the SST $k-\omega$ model for adjoint calculation. In Proceedings of the 54th AIAA Aerospace Sciences Meeting, San Diego, CA, USA, 4–8 January 2016. [[CrossRef](#)]
58. Spalart, P.R.; Rumsey, C.L. Effective Inflow Conditions for Turbulence Models in Aerodynamic Calculations. *AIAA J.* **2007**, *45*, 2544–2553. [[CrossRef](#)]
59. Castillo, R.; Pol, S. Wind tunnel studies of wind turbine yaw and speed control effects on the wake trajectory and thrust stabilization. *Renew. Energy* **2022**, *189*, 726–733. [[CrossRef](#)]
60. Maldonado, V.; Castillo, L.; Thormann, A.; Meneveau, C. The role of free stream turbulence with large integral scale on the aerodynamic performance of an experimental low Reynolds number S809 wind turbine blade. *J. Wind. Eng. Ind. Aerodyn.* **2015**, *142*, 246–257. [[CrossRef](#)]

61. Brandt, J.; Selig, M. Propeller Performance Data at Low Reynolds Numbers. In Proceedings of the 49th AIAA Aerospace Sciences Meeting including the New Horizons Forum and Aerospace Exposition, Orlando, FL, USA, 4–7 January 2011. [[CrossRef](#)]
62. Ananda, G. UIUC Propeller Database, Volume 1, 2015. Available online: <https://m-selig.ae.illinois.edu/props/volume-1/propDB-volume-1.html> (accessed on 15 October 2022).
63. Traub, L.W. Range and Endurance Estimates for Battery-Powered Aircraft. *J. Aircr.* **2011**, *48*, 703–707. [[CrossRef](#)]

Disclaimer/Publisher’s Note: The statements, opinions and data contained in all publications are solely those of the individual author(s) and contributor(s) and not of MDPI and/or the editor(s). MDPI and/or the editor(s) disclaim responsibility for any injury to people or property resulting from any ideas, methods, instructions or products referred to in the content.